

# **Ground Truthing Earth's Silicate Weathering Thermostat: Using the Geochemistry of Himalayan Groundwaters to Calculate Residence Times**

Giovanni Bernardi

Part III Project

2024-2025



# **Abstract**

IMO, the abstract should be a supercondensed version of the paper.

Grab the readers attention -> why we care about the topic

What's the unknown? Are fluids actually following the Maher model?

How did you do this? Collected samples, tested models.

What did you find? The Maher model isn't appropriate etc

Loop back into the original part about why we care and the unknown. Has it been answered? What are the implications?

Residence time calculations determined using rate constants close to equilibrium give ages of order ten years for the model which purports discharge to be the greatest control on weathering. The other model, following the null hypothesis that temperature is the greatest control on weathering, gives residence times of a similar order of magnitude but the assumption of a constant rate of reaction is likely unrealistic. Simple calculations based on yearly rainfall support the residence time obtained by both models. Estimates of free energy suggest that the weathering reactions contributing to the dissolved load in the groundwater are not close to equilibrium. As a result, it is unlikely that the fast rates of reaction used are appropriate for catchments like Melamchi. Furthermore, this suggests that the main assumption of the Maher model is not valid in this catchment. These analyses suggest that a combination of both models' is necessary to accurately model a real catchment like Melamchi.

# Contents

<b>Abstract</b>	i
<b>1 Introduction</b>	1
<b>2 Study Area</b>	6
2.1 Geology and Geomorphic Setting . . . . .	6
2.2 Climate . . . . .	6
<b>3 Data Collection and Measurement</b>	8
3.1 Field Sampling . . . . .	8
3.2 Major and Trace Element Analysis . . . . .	8
3.3 Isotope Analysis . . . . .	8
<b>4 Methods and Models for Analysis</b>	9
4.1 Rain and Hydrothermal Correction . . . . .	9
4.2 Modal Decomposition Identifies Weathering Reaction . . . . .	9
4.3 One-Dimensional Reactive Transport Models . . . . .	12
4.4 Estimates of Uncertainty . . . . .	17
<b>5 Results: Differences in Spring Chemistry and Residence Time</b>	18
5.1 Traverse 1 . . . . .	18
5.2 Traverse 2 . . . . .	20
5.3 Traverse 3 . . . . .	22
5.4 Traverse 4 . . . . .	24
5.5 Traverse 5 . . . . .	26
5.6 Time Series Trends . . . . .	27

<b>6 Discussion</b>	<b>28</b>
6.1 Explaining Traversal Variations in Chemistry . . . . .	28
6.2 Strontium Isotopes suggest Little Rainwater Influence . . . . .	30
6.3 Model Constraints on Residence Time . . . . .	33
6.4 Free Energy Calculations . . . . .	36
<b>References</b>	<b>40</b>
<b>Appendix 1: Strontium Isotopes Mass Balance Mixing Model</b>	<b>48</b>
<b>Appendix 2: Rain and Hydrothermal Correction Equations</b>	<b>49</b>
<b>Appendix 3: Derivation of Reactive Transport Models</b>	<b>51</b>

## **Acknowledgements**

This thesis would not have been possible without the amazing help from my supervisor, Ed Tipper. Mike Bickle and Al Knight and Morag Hunter have also been instrumental in guiding me through this Master's year. To Zara, I couldn't ask for a better field partner. To my friends and peers, thank you for supporting me throughout. A Mamma, Papà, e la Virgi, grazie di tutto come sempre. Finally, to Beth, I couldn't have done this without you.

## **List of Tables**

# **Nomenclature**

# 1 Introduction

Silicate weathering, whereby silicate minerals are dissolved by carbonic acid, sequesters atmospheric CO<sub>2</sub> over long (10<sup>6</sup> year) timescales, influencing global climate regulation. As water passes through the subsurface, it interacts with the surrounding rock. This causes the addition of solute species to the groundwater, and the formation of stable secondary minerals through the dissolution of primary minerals formed at different pressure and temperature. The Himalayan mountain range spans more than 590,000 km<sup>2</sup>, and is the source of major rivers, including the Ganges, Brahmaputra, and Indus. It is therefore a key region for understanding the global carbon cycle. In highly erosive regions where the supply of silicate minerals far exceeds the weathering rate, silicate weathering reactions are thought to be sensitive to climate. These regions are called "kinetically-limited" (Stallard & Edmund 1983 JGR, West et al, 2005) The dissolution kinetics of the silicate rocks in these catchments are thought to be sensitive to temperature and runoff because the weathering reactions have not gone to completion. Silicate weathering in the Himalayas as a result of their uplift and erosion in the Cenozoic may have contributed significantly to the global cooling over the past 40 million years (Raymo and Ruddiman, 1992; West et al, 2005, Kump et al, 2000 Ann Rev Earth Sci). Thus, it is this reported sensitivity to climate as well as their large size that makes them important to study. Models built on this sensitivity ("Fontorbe models" from now on) are used to simulate groundwater through one-dimensional flow paths based on a few key parameters, which make up the "weathering fingerprint" of a catchment (Fontorbe et al., 2013). More recent models have proposed silicate weathering is more sensitive to the hydrological cycle, than to temperature (Maher, 2011). The underlying assumption in these ("Maher models" from now on) is that all weathering paths approach equilibrium. If equilibrium is indeed approached in a particular catchment, then the Maher model is more suitable for use.

The weathering fingerprints of these catchments contain many unknowns, namely the residence time of the water, flow path direction and length, rate of reaction, and extent to which equilibrium is reached. Understanding residence time in particular is important be-

cause the geochemical and biogeochemical reactions that are used to quantify weathering are time-dependent; longer residence times promote greater solute accumulation in the water (Berner, 1978). These geochemical reactions are also controlled by the reaction rate which is thought to vary as equilibrium is approached (White and Brantley, 2003; Maher, 2011). Therefore, an understanding of residence time will provide insight into how long weathering reactions take place in a given catchment, whether they reach equilibrium, and what this means for the carbon cycle as a whole. Residence time will also reflect the variety of flow routes within a catchment because of physical constraints like Darcy's law, which will help to improve hydrological models. The aim of this study is to compare the Fontorbe and Maher models and their estimation of residence time, and assess their applicability to a real-world catchment.

From the model comparison will come a better understanding of fluid residence times in Himalayan catchments, for which tracer data is already commonly used to infer how long a water packet spends in the subsurface (Atwood et al, 2021). Previous studies on Melamchi have used CFC and SF<sub>6</sub> gases to determine a mean age on the order of ten years for groundwater at the base of the catchment ridge (Atwood et al, 2021). Using the chemical composition of the water will provide a different way of obtaining residence times, and give a benchmark for the tracer data, which is often reported to be limited in its application (McCallum et al, 2015). If the residence time of a particular water packet is long enough, the reaction will reach chemical equilibrium, meaning the free energy of the system will be close to zero. Comparison of these residence times with estimates of free energy derived from the measured concentration of springwater in the catchment will provide a test on the validity of the two models and their assumptions.

The rate of weathering is dependent on the mineralogy of the rock. Different minerals weather at different rates: quartz > albite > mafic silicates > anorthite > carbonates. Therefore, the most reactive minerals will contribute disproportionately to the solute load of the water (Shand et al, 1999). In the Melamchi catchment, only weathering through carbonic acid is considered. Weathering through sulfuric acid is also a big player in the global

weathering budget, but its impact is not considered in this study because the marine deposits required for its formation are not present in the Melamchi region (Bufo et al., 2021). Differences in lithology are thought to affect weathering. Geological differences lead to differences in soil composition, landscape features, vegetation, and climate which in turn affect the rates of reaction. Logically, the contribution of one lithology to weathering is correlated to its spatial extent in the catchment (Stallard and Edmond, 1983). Porosities vary widely across a catchment depending on the rock type encountered (Singh et al, 1987; David et al, 1994). Porosity also increases as a rock becomes more weathered (Marques et al, 2009). Weathering regimes can be classified as either transport-limited or kinetically limited (West et al., 2005). West et al. (2005) distinguish the two regimes by the rate of erosion in the catchment. In low erosion rate settings, weathering is transport-limited due to limited mineral supply. Weathering here is therefore proportional to the material eroded. In high erosion rate settings, weathering is kinetically-limited due to an abundant mineral supply. Rapidly eroding catchments like Melamchi are therefore likely kinetically-limited. Soil properties and topography are used to identify different "weathering regimes" in the subsurface (Pedrazas et al, 2021). Indeed, bedrock strength is thought to be more dependent on weathering than mineral or textural differences between the metamorphic lithologies in the Himalayas (Medwedeff et al, 2021). Understanding the extent of weathering can therefore serve to predict the stability of bedrock in rapidly eroding regions.

The strontium isotope composition of different rock types is indicative of different formation mechanisms and conditions. This is used to track the relative contributions of weathering and hydrothermal circulation inputs in seawater (Edmond, 1992). The rock signature imparts a strontium isotopic composition to groundwater that reacts with it in the subsurface. Hence, measuring the strontium isotopic composition of groundwater can provide information on provenance and mixing between streams that react with different lithologies (Faure, 2001).

Rates of reaction during weathering comprise both dissolution and precipitation, and chemical equilibrium is defined as that state where these are balanced and equal. Rates of

reaction are thought to be different depending on whether they are measured in the field or in a laboratory (Maher et al., 2009). This difference has been explained by denoting 'extrinsic' qualities that are variable in the field, such as permeability and mineral/fluid ratios (White and Brantley, 2003). The rate of reaction of a system has also been linked to the free energy of the system, with laboratory rates being calculated significantly further away from equilibrium than field rates (Kampman et al, 2009). This implies that field localities are closer to equilibrium than laboratory-derived rates might suggest.

The Indian Summer Monsoon (ISM) in Nepal is characterised by a strong seasonal reversal of winds, which brings heavy rainfall to the region during the summer months, and dry conditions during the winter (Bookhagen and Burbank, 2010). The monsoon brings a large amount of precipitation to the region. Oxygen isotopes suggest most of the precipitation occurs in the higher elevation parts of the catchment, and this is supported by remotely sensed rainfall estimates in the region (Acharya et al, 2020; Bookhagen and Burbank, 2010). Precipitation and discharge relationships in the Himalayas have been used to suggest that there is a three month lag in the response of the river to precipitation (Andermann et al., 2012). The residence time of groundwater can be used to quantify this delay and nature of its origin, given that rain is the main source of recharge to the groundwater system (Illien et al, 2021). Studying small catchments gives the opportunity to attribute large changes in water chemistry to seasonal climate changes like the monsoon (Tipper et al., 2006). Seasonal variation in rainfall is thought to relate to different hydrological regimes, whereby river discharge and precipitation are 'coupled' when there is a significant enough amount of water to recharge the groundwater system. (Illien et al, 2021) The seasonal variation in precipitation therefore also translates to a variation in runoff, whereby this is twelve times stronger during the monsoon than during the dry season (Sharma, 1997).

Changes in climate contribute to changes in the monsoonal system dynamics. The start of the monsoon has not changed in Nepal, but the end has been delayed. This has led to more intense precipitation on a per day basis, which is detrimental for crops in the winter season due to lack of moisture. Intense precipitation is also considered the main climatic

cause of flooding (Panahi et al, 2015; Baniya et al, 2012). "One-off" landslide events transport as much as four times the flux of sediment deposited in the valley in a year (Chen C et al., 2023). These events are thought to be increasing in frequency over recent years as a result of climate change, increasing the erosion rate in these areas (Adhikari et al, 2023). In particular, effects of a flash flood in 2021 are still visible in the area, with damage done to several bridges and hundreds of families.

In this study, spring and rain samples from the Melamchi region of Nepal are used as a case study to investigate the weathering rates in a kinetically-limited catchment. The sample dataset consists of 372 samples spanning four field campaigns over three years (2021-2024), as well as more recent year-long bi-weekly timeseries data from stream and spring samples in sites across the catchment. Of those, 68 were collected in September 2024 for this study. This dataset comprises major ion concentrations, alkalinity, and radiogenic strontium isotopes from the Melamchi catchment.

## **2 Study Area**

The Melamchi-Indrawati catchment (85.441 - 85.601 E, 27.822 - 28.157 N) study area ranges from 790 to 5700 m a.s.l. (metres above sea level). The Melamchi River is a tributary of the larger Indrawati River and runs through the catchment draining an area of 325km<sup>2</sup>.

### **2.1 Geology and Geomorphic Setting**

The geology of Melamchi is characterised by the characteristic banded gneiss, feldspathic schist and laminated quartzite of the Higher Himalayan Crystalline Sequence (HHCS). To the south of the confluence of the Melamchi River to its parent Indrawati river lies the Main Central Thrust (MCT) which separates the HHCS from the Lower Himalayan Sequence (LHS) (Dhital et al, Graf et al). The overall geology is therefore largely comprised of silicate metamorphic rock. (map)

### **2.2 Climate**

Annual mean temperatures in the Melamchi Khola Catchment range from 24°C at base elevation to 8°C at highest elevation sampled (3200 m a.s.l.). The area is characterised by a high erosion rate. The southern Himalayas are characterised by a large topographic gradient. This corresponds to a large temperature gradient contributing to tropical and alpine climates close to one another (Kattel et al, 2012). The westerly winds typical of this latitude are responsible for the dry season in the Himalayas (Bookhagen and Burbank, 2010). The source of precipitation during the Indian Summer Monsoon (ISM) affecting Melamchi is the Bay of Bengal, due to the strong pressure gradient that changes the westerly winds to southerly winds. This temperature gradient reverses in the winter, when the oceans are warm and the High Himalaya is cold. The Melamchi Khola catchment receives over 80% of its rainfall during the monsoon.

Recorded temperatures at the end of the spring flow paths vary with the season, being coldest in November. All seasons show a temperature decrease with increasing elevation,

consistent with the free-air moist adiabatic lapse rate, which is = 6.5 °C/km (Barry and Chorley, 2009). This differs from the annual mean lapse rate in the southern Himalayas of = 5.2 °C/km (Kattel et al., 2013). This disparity could be due to the fact that temperatures may be warmer than air temperatures because of radiative heating. The difference may also be due to systematic errors in temperature measurements; between collection and sampling, warming of the water is plausible.

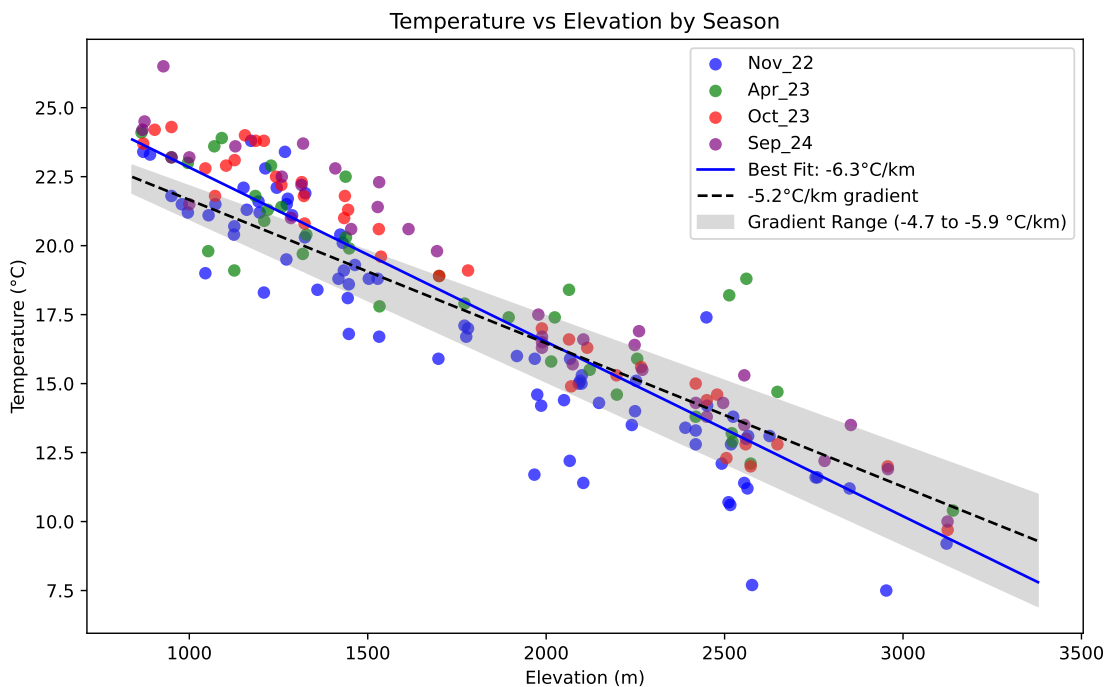


Figure 1: Temperature changes

Catchment	Area	Mean	Mean Ele-	Elevation	Geology	Location	Range
		Slope	vation	Range	(DD)		
	(km <sup>2</sup> )	(%)	(m)	(m)			
Melamchi Khola	325	20	2400	786–5697	HHCS	85.441–85.601 E 27.822–28.157 N	

Table 1: Catchment characteristics of the study area.

### **3 Data Collection and Measurement**

#### **3.1 Field Sampling**

Both springs and rain were sampled in the field. Springs were sampled according to locations visited in past expeditions. Rain was collected in a rain gauge along several transects. Both water bodies were measured in the field for temperature, pH and TDS on a Hanna Instruments HI-991300 and EXTECH DO700. Samples were also titrated using a Hach digital titrator with 0.0625M HCl to calculate the alkalinity of the water following the Gran Method (Gran, 1952). The field measurements were done 24 hours within having been collected. Six aliquots were collected for each spring for anion, cation, titration, DIC, isotope and archive purposes respectively. Rain samples had a smaller yield and so only three aliquots were collected, for ion, isotope and archive purposes. Both water body types were filtered through a  $0.2\mu\text{m}$  PES membrane in a filtration unit prior to bottling. Cation and archive samples were acidified with concentrated  $\text{HNO}_3$  to give a pH of  $\sim 2$ , keeping the cations in solution.

#### **3.2 Major and Trace Element Analysis**

Cation concentrations were determined using a Agilent Technologies 5100 Inductively-Coupled Plasma Optical Emission Spectrometer (ICP-OES) using a calibration line made from a Nepalese spring stock solution. Anion concentrations were determined using a Dionex Ion Chromatography System (ICS) 5000 series against the Battle-02 standard calibration line. Associated uncertainties range between 5-10% for cations and anions.

#### **3.3 Isotope Analysis**

Samples for radiogenic strontium analysis were dried down to provide at least 100 ng of Sr. Samples were then dissolved in aqua regia (3:1  $\text{HNO}_3:\text{HCl}$ ) to remove any additional organic matter. Once dried down again, they were added to 3 ml teflon columns with Eichrom SrSpec<sup>®</sup> resin pipetted in. Once washed three times with Milli-Q<sup>®</sup> water, the column was

primed with 3M HNO<sub>3</sub>. The sample was centrifuged then loaded onto the column avoiding any solids. The column was then washed a total of three times with 3M HNO<sub>3</sub> to remove other cations. Lastly, the column was eluted to a beaker with Milli-Q® water to collect the Sr. Once dried, the samples were dissolved in 3M HNO<sub>3</sub>, centrifuged and then diluted for analysis on a Thermo Scientific Neptune Plus MC-ICP-MS. Errors on Sr isotope measurement are taken from two standard deviations of the measured values given by the MC-ICP-MS.

## 4 Methods and Models for Analysis

### 4.1 Rain and Hydrothermal Correction

Rain input is a significant factor in the chemical composition of groundwater and rivers. Most chloride found in these water bodies is thought to be due to rainwater input (Drever, 1997). It is standard practice to correct for this rain input. Once the samples have been corrected for rain input, the remaining chloride is assumed to be derived from hydrothermal signatures encountered in the flow path. Spring waters are also therefore corrected for hydrothermal input, so that the concentrations used for modelling are strictly derived from weathering reactions.

### 4.2 Modal Decomposition Identifies Weathering Reaction

The first step towards quantifying the extent to which chemical weathering reactions have gone to completion is to discern what reaction is taking place. In principle this is as simple as knowing what minerals are dissolving and which are precipitating. Modal decomposition methods consider several minerals that could be dissolving and/or precipitating, and their stoichiometry (Garrels and Mackenzie, 1967; Drever, 1997). Note that this calculation can only be done if the number of components is the same as or greater than the number of minerals.

$$\begin{array}{ccccccc}
& Biot & Plag & Calc & Smec & Kaol & Kspar \\
\begin{matrix} Si \\ Al \\ Mg \\ Ca \\ Na \\ K \end{matrix} & \left( \begin{array}{cccccc} a_{11} & a_{12} & a_{13} & a_{14} & a_{15} & a_{16} \\ a_{21} & a_{22} & a_{23} & a_{24} & a_{25} & a_{26} \\ a_{31} & a_{32} & a_{33} & a_{34} & a_{35} & a_{36} \\ a_{41} & a_{42} & a_{43} & a_{44} & a_{45} & a_{46} \\ a_{51} & a_{52} & a_{53} & a_{54} & a_{55} & a_{56} \\ a_{61} & a_{62} & a_{63} & a_{64} & a_{65} & a_{66} \end{array} \right) & \cdot & \left( \begin{array}{c} x_{Biot} \\ x_{Plag} \\ x_{Calc} \\ x_{Smec} \\ x_{Kaol} \\ x_{Kspar} \end{array} \right) & = & \left( \begin{array}{c} b_1 \\ b_2 \\ b_3 \\ b_4 \\ b_5 \\ b_6 \end{array} \right)
\end{array}$$

Matrix algebra facilitates the calculations of the mineral proportions in the water. Given known matrices  $A$  and  $B$ , where  $A$  represents the stoichiometric quantities of elements in a mineral, and  $B$  the concentrations of elements in the water:

$$AX = B \quad (1)$$

$$X = A^{-1}B \quad (2)$$

The matrix  $X$ , corresponding to volumetric proportions of the minerals in the water, can then be calculated, under the assumptions that all minerals dissolve in a congruent fashion. Modal decomposition for spring waters was performed according to stoichiometric proportions from Bickle et al. (2015). For ease of visualisation, Figure 2 shows the positive, dissolved minerals on the LHS, and the negative, precipitated minerals on the RHS.

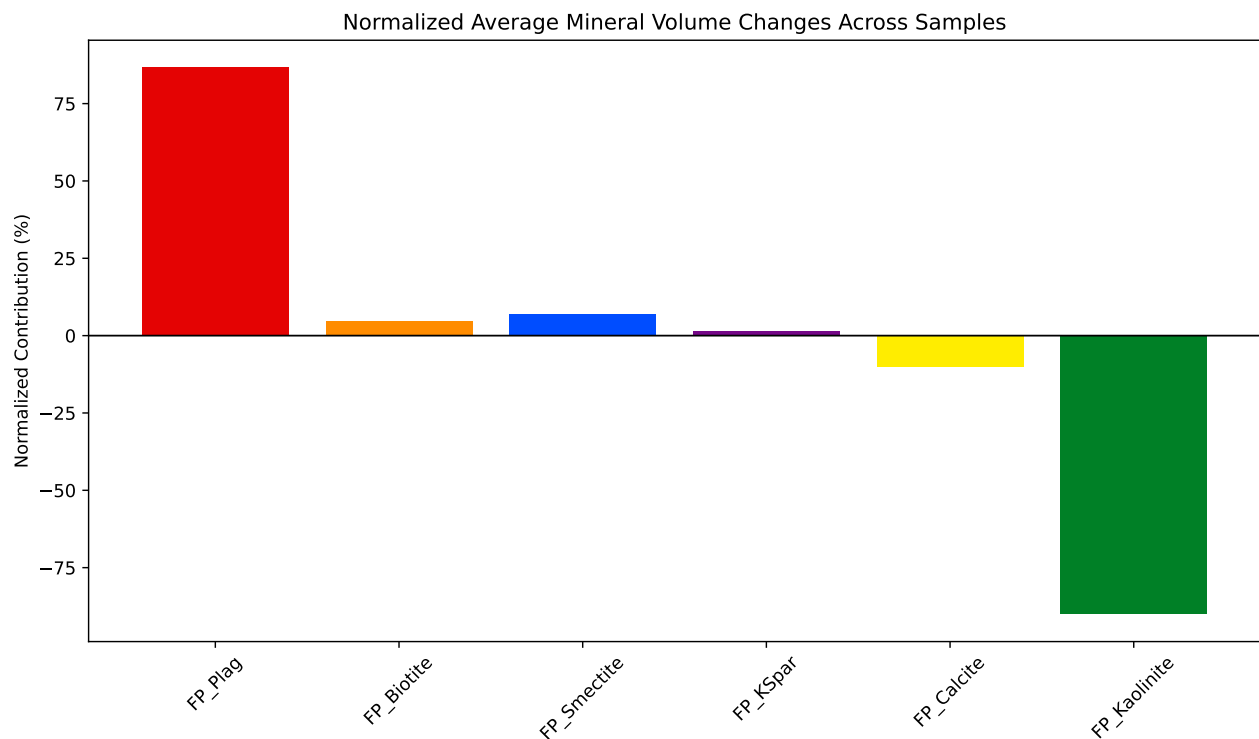
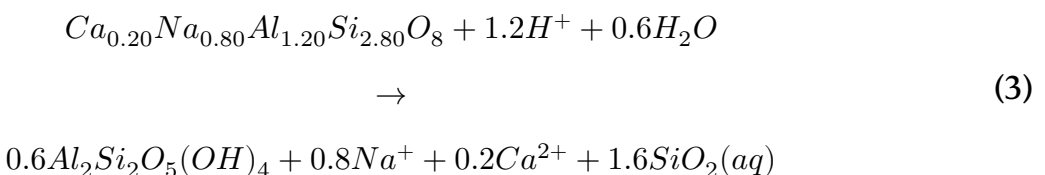
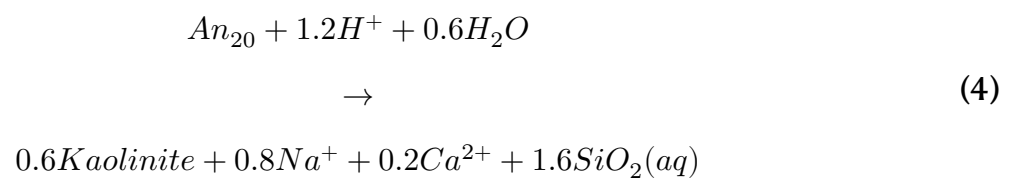


**Figure 2: Average of the modal decomposition for the springs in Traverse 3.**

Figure 2 is representative of most springs in Traverse 3. Hence, the major phase being dissolved is plagioclase feldspar and the major phase being precipitated is kaolinite. The primary composition of plagioclase in the area corresponds to  $\approx$  An-20 (Bickle et al., 2015; Knight et al., 2024). The plagioclase to kaolinite reaction is given by the following equation (written so that aluminium is conserved):



Or



## 4.3 One-Dimensional Reactive Transport Models

Reactive transport models are widely used in applied fluid dynamics and various fields within Earth Sciences. These models aim to track chemical reactions occurring at each spatial point, accounting for the movement of reactants to and reaction products away from those points (Bethke, 2011). The basic form of a reactive transport model is a partial differential equation that describes the transport of solutes and the reactions that occur between them. For reacting solutes, concentration changes over time are governed by transport rates – derived from the divergence principle – and the relative rates of dissolution and precipitation (Bethke, 2011). The proposed equations can be complex, but in simple cases a species of concentration  $C_i$  can be modelled to follow a first-order rate law, generally represented by:

$$\frac{\partial C_i}{\partial t} = \mathcal{O}_T(C_i) + \mathcal{O}_R(C_i) \quad (5)$$

Where  $\mathcal{O}_T$  and  $\mathcal{O}_R$  are the transport and reaction operators, respectively (Bethke, 2011). Depending on the hypothesis supported, equation 5 can be modified accordingly. The following sections will discuss two models with their own versions of equation 5.

### Model Motivation

As discussed in the Introduction (ref), there are different hypotheses regarding the major controls on chemical weathering. This section will contrast one model following the null hypothesis that weathering is largely sensitive to climate and temperature (Fontorbe et al., 2013), and another model that suggests weathering is more sensitive to fluid flux (Maher, 2011; Maher and Chamberlain, 2013). Given the emphasis on deriving fluid residence times from solute concentrations, the benchmark for a model's effectiveness will be how well it can predict these times compared to previous studies on gas tracers and simple box models. Assumptions and constraints will be compared and contrasted, and their results used to inform the calculation of rates of reaction and approach to equilibrium in Melam-

chi. For both models, the element used to benchmark is dissolved silicon. This is because silicon is present in both dissolution and precipitation reactions, so it is applicable to the Maher model which considers both reactions. Furthermore, silicon is what both models were used for in their respective original studies.

### **Fontorbe et al. (2013) - Model**

This model investigates silicon isotopic composition in the Ganges River, assuming constant reaction rates along flow paths (see Appendix for a full derivation, and Table ref for a list of parameters used). The first-order differential equation governing transport and reaction is given as:

$$\phi \frac{\partial C}{\partial t} = -\omega \phi \frac{\partial C}{\partial z} + R_n(1-f) \quad (6)$$

Where  $C$  is the elemental concentration,  $\omega$  is the fluid velocity,  $\phi$  is the rock porosity,  $z$  is a position along the flow path,  $R_n$  is the rate of reaction, and  $f$  is the fraction of Si present in the dissolved load that is reprecipitated in the back reaction. The equation can be nondimensionalised using the Damköhler number ( $N_D$ ), which describes the relative importance of kinetic vs transport-controlled settings (Bethke, 2008):

$$N_D = \frac{R_n h}{\phi C_0 \omega} \quad (7)$$

Assuming steady-state ( $\partial C / \partial t = 0$ ), the concentration at the end of the flow path can be rearranged to give the residence time  $T_f$ :

$$T_f = \frac{(C - C_0)\phi}{(1 - f)R_n} \quad (8)$$

<b>Fontorbe</b>			
<b>Parameter</b>	<b>Definition</b>	<b>Units</b>	<b>Formula (Value)</b>
$\phi$	Porosity	-	0.1*
$\omega$	Fluid velocity	m/s	Variable
$h$	Length of flow path	m	Variable
$C$	Concentration end of flow path	$\mu\text{mol/L}$	Variable
$C_0$	Initial concentration	$\mu\text{mol/L}$	Rain Input
$f$	Fraction reprecipitated	-	0.5*
$N_D$	Damkohler Number	-	$N_D = \frac{R_n h}{\phi C_0 \omega}$
$T_f$	Residence time	s	$T_f = \frac{h}{\omega \phi}$
$R_n$	Reaction rate	$\text{mol}/\text{m}^3/\text{s}$	$\rho \cdot 10^6 \cdot k \cdot S \cdot X$
$k$	Reaction rate constant	$\text{mol}/\text{m}^2/\text{s}$	$10^{-15*}$
$S$	Specific surface area	$\text{m}^2/\text{g}$	0.1*
$\rho$	Plagioclase density	$\text{g}/\text{cm}^3$	2.7*
$X$	Volume fraction of mineral in rock	$g_{\text{min}}/g_{\text{rock}}$	0.2*

Table 2: Key parameters and definitions for the Fontorbe model. Starred terms are values used for calculation.

## Maher and Chamberlain (2014) Model

This model is built in accordance with the principle that the main control on silicate weathering is the residence time of the water. The model is based on the assumption that the reaction rate decreases linearly with approach to equilibrium, and that all weathering paths approach equilibrium. The motivation behind the hydrological control is based on sensitivity analyses of real catchment data on one-dimensional reactive transport models which suggest that porosity, mineral surface area, and temperature have no consistent correlation with water composition (Maher, 2011). See Appendix and Table ref for a full derivation and the model parameters respectively. The model begins with the following representation of the concentration of a solute in a fluid flow path:

$$\frac{dC}{dt} = -\frac{q}{\theta} \frac{dC}{dz} + \sum_i \mu_i R_{d,i} \left(1 - \left(\frac{C}{C_{eq}}\right)^{n_i}\right)^{m_i} - \sum_i \mu_i R_{p,i} \left(1 - \left(\frac{C}{C_{eq}}\right)^{n_i}\right)^{m_i} \quad (9)$$

Where  $C$  is the concentration,  $q$  is the fluid flux,  $\theta$  is the volumetric water content,  $z$  is the position along the flow path,  $\mu$  is the stoichiometric coefficient,  $R$  is the rate of reaction for dissolution and precipitation respectively,  $C_{eq}$  is the equilibrium concentration, and  $n$  and  $m$  are non-linear parameters (Maher and Chamberlain, 2013). For a given packet of water,  $R_n$  is defined as:

$$R_n = R_d - R_p \quad (10)$$

$$\frac{dc}{dt} = R_n \left(1 - \frac{C}{C_{eq}}\right) \quad (11)$$

Where  $R_d$  and  $R_p$  are the rates of dissolution and precipitation respectively. This can be solved for concentration, and rearranged for residence time to obtain:

$$T_f = \frac{C_{eq} \cdot (C - C_0)}{e^2 R_n (C_{eq} - C)} \quad (12)$$

Note the  $e^2$  term is used because the Maher model considers all paths as if they approach equilibrium.

<b>Maher</b>			
<b>Parameter</b>	<b>Definition</b>	<b>Units</b>	<b>Formula (Value)</b>
$\phi$	Porosity	-	0.1*
$h$	Length of flow path	m	Variable
$q$	Flow rate	m/s	Variable
$C_{eq}$	Equilibrium concentration	$\mu\text{mol/L}$	Max Catchment
$C_0$	Initial concentration	$\mu\text{mol/L}$	Rain Input
$R_n$	Net reaction rate	$\text{mol/L/s}$	$\rho \cdot 10^6 \cdot k \cdot S \cdot X$
$\rho$	Plagioclase density	$\text{g/cm}^3$	2.7*
$k$	Reaction rate constant	$\text{mol/m}^2/\text{s}$	$10^{-15*}$
$S$	Specific surface area	$\text{m}^2/\text{g}$	0.1*
$X$	Volume fraction of mineral in rock	$g_{min}/g_{rock}$	0.2*
$\tau$	Scaling factor	-	$\tau = e^2$
$D_w$	Damkohler Coefficient	$\text{m}^2/\text{s}$	$D_w = \frac{L\phi R_n}{C_{eq}}$
$T_f$	Residence time	s	$T_f = \frac{h\phi}{q}$

Table 3: Key parameters and definitions for the Maher model. Starred terms are values used for calculation.

## 4.4 Estimates of Uncertainty

Uncertainties were propagated using a Monte Carlo method using an assumed normal distribution. Both the observed parameters and estimated parameters have uncertainties associated to them.

Parameter Definitions and Propagated Uncertainties				
Parameter	Definition	Units	Value	Uncertainty
$\phi$	Porosity	-	0.1	$\pm 10\%$
$C_{eq}$	Equilibrium DSi concentration	$\mu\text{mol/L}$	$869 \mu\text{mol/L}$	$\pm 10\%$
$C_0$	Initial DSi concentration	$\mu\text{mol/L}$	$95 \mu\text{mol/L}$	$\pm 10\%$
$\rho$	Plagioclase density	$\text{g/cm}^3$	2.7	$\pm 10\%$
$k$	Reaction rate constant	$\text{mol/m}^2/\text{s}$	$10^{-15}$	$\pm 10\%$
$S$	Specific surface area	$\text{m}^2/\text{g}$	0.1	$\pm 10\%$
$X$	Volume fraction of mineral in rock	$\text{g}_{\text{min}}/\text{g}_{\text{rock}}$	0.2	$\pm 10\%$
$f$	Fraction reprecipitated	-	0.5	$\pm 10\%$
$\Delta G^0$	Standard Gibbs Free Energy	$\text{kJ/mol}$	$-\text{RTlnK}^*$	$\pm 10\%$

Table 4: Key parameters, definitions, and propagated uncertainties. \* Uncertainty associated with temperature and K calculated from pgcc using The Geochemist's Workbench® Rxn program(ref)

# 5 Results: Differences in Spring Chemistry and Residence Time

## 5.1 Traverse 1

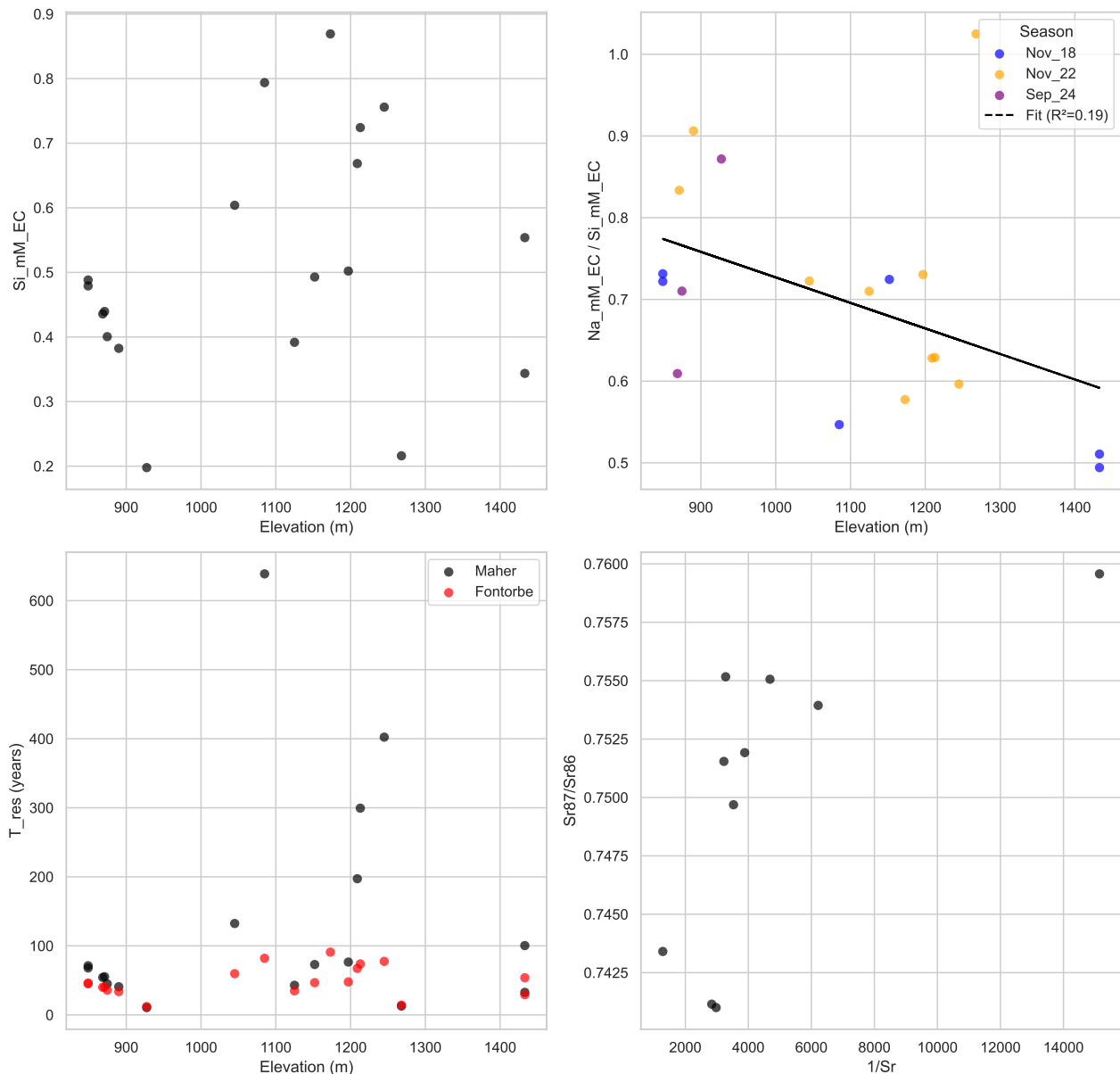


Figure 3: Traverse 1 - Variations in Spatial Chemistry

Concentration of dissolved silicon (DSi) in the springs sampled in Traverse 1 is at a maximum for the whole catchment. There is no clear trend of increasing DSi concentration with decreasing elevation, but Na/Si does increase with the same x-axis. The Fontorbe model

predicts a peak of  $\approx$  100 years, while the Maher model predicts a much higher residence time of  $\approx$  600 years. Strontium isotopes are also at a maximum in this traverse, but there is no resolvable mixing trend; strontium isotope ratios used alongside strontium concentrations can be used to determine mixing between different endmembers (Faure, 1986; See Appendix).

## 5.2 Traverse 2

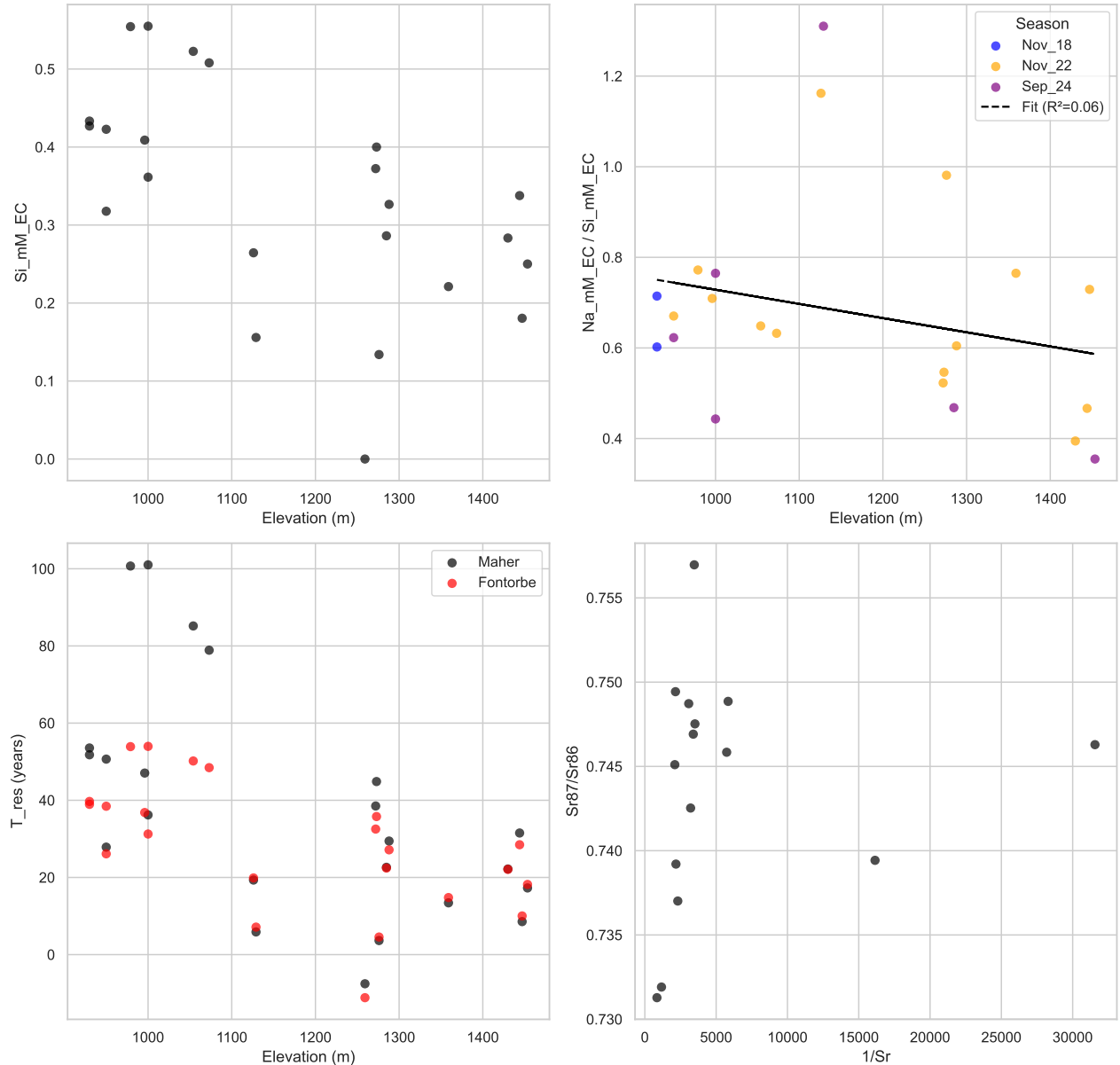


Figure 4: Traverse 2 - Variations in Spatial Chemistry

Dissolved silicon concentration shows a clear increase in concentration with decreasing elevation. There is no resolvable trend with  $\text{Na}/\text{Si}$  and elevation, nor with different seasons when it was collected. Residence times are generally lower than those in Traverse 1, but the Maher model is still higher at lower elevations, predicting a maximum of  $\approx 100$  years. The Fontorbe model predicts generally older times than the Maher model at higher elevations, and lower times at lower elevations. Strontium isotopes are in the same range

as those in Traverse 1. Here, a mixing trend is resolvable given by a straight line with a  $R^2$  of (?).

### 5.3 Traverse 3

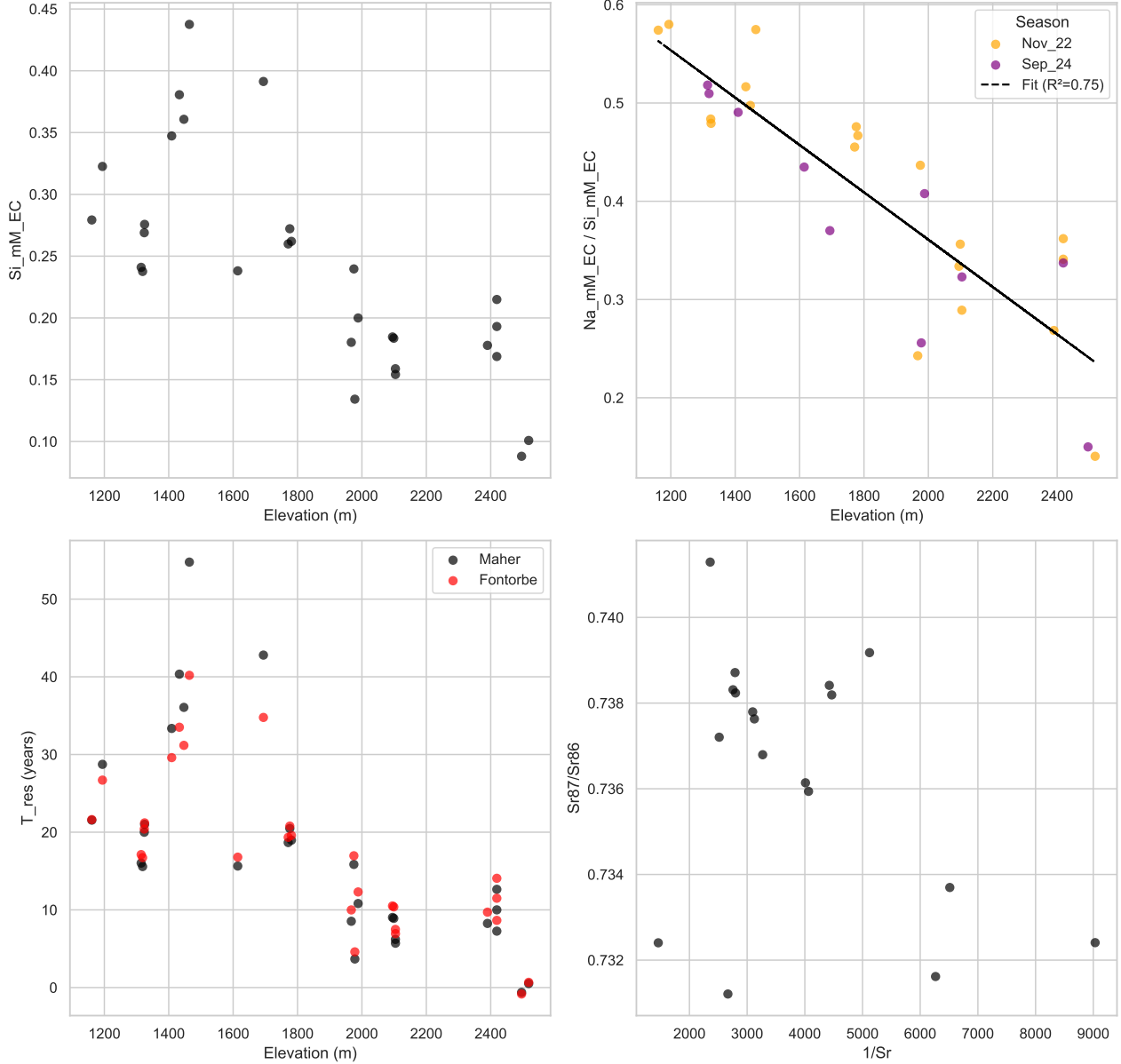


Figure 5: Traverse 3 - Variations in Spatial Chemistry

Dissolved silicon concentration increases with decreasing elevation in Traverse 3. There is a potential dip at the lowermost elevation sampled. Na/Si showcases a consistent increase with decreasing elevation, and this trend carries through between different seasons. Residence times predicted increase as elevation decreases, peaking at  $\approx 50$  years for the Maher model. At the very end of the flow path, however, both the Maher and Fontorbe model predict  $\approx 25$  years. Strontium isotopes do not showcase a clear mixing trend, and

the radiogenic strontium isotope values are lower than those found in Traverse 1 and 2.

## 5.4 Traverse 4

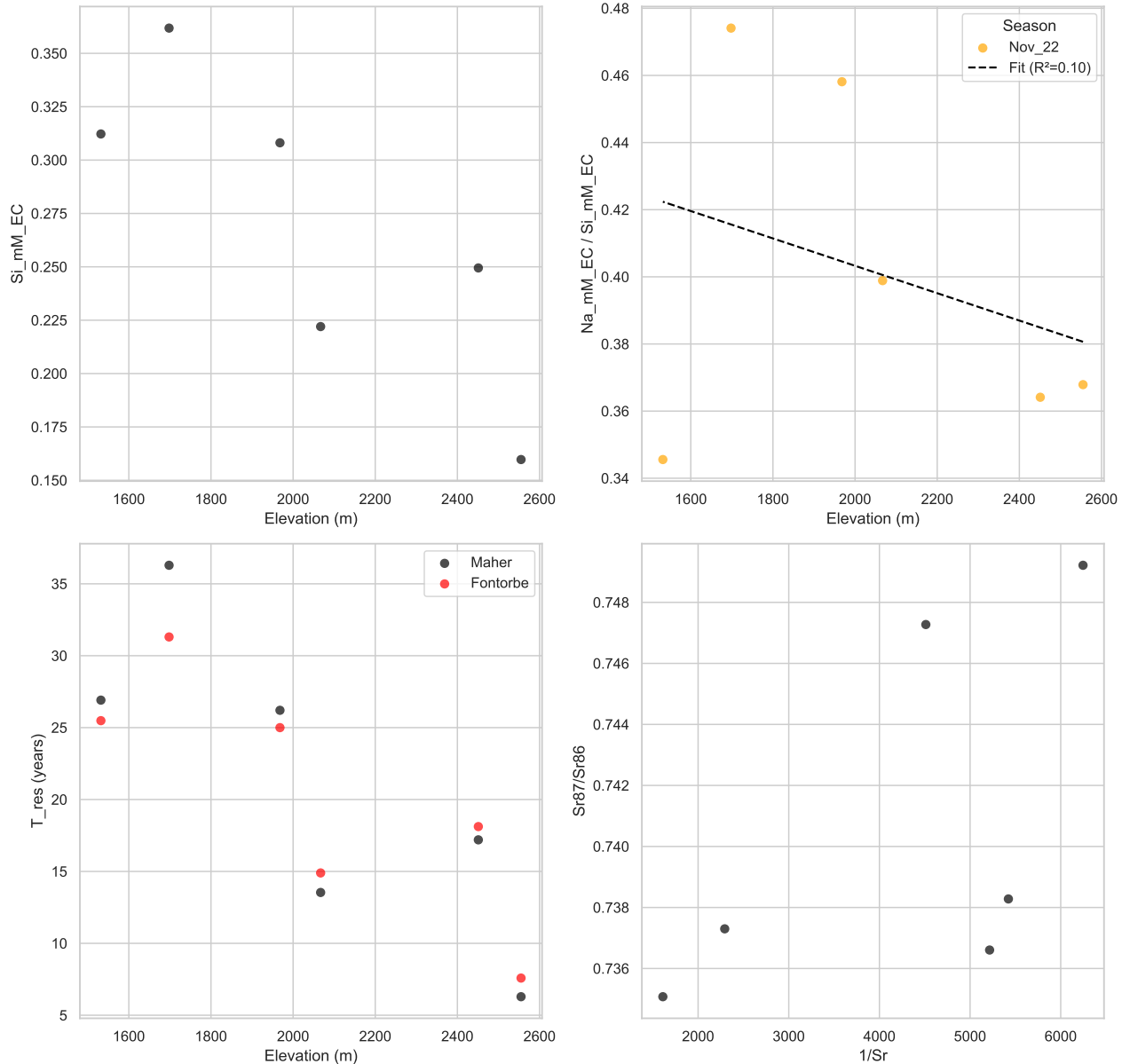


Figure 6: Traverse 4 - Variations in Spatial Chemistry

Traverse 4 is undersampled compared to the other traverses. Given the small sample set, any apparent trend is less likely to be reflective of the true chemistry. Nevertheless, DSi increases with decreasing elevation as seen in some of the previous traverses. There is no discernable trend with Na/Si. Residence times also increase with decreasing elevation, with the Maher model predicting younger times at the highest elevations, and older times at the lowest elevations. The highest residence times predicted are  $\approx 35$  years. Strontium

isotopes do not show a clear mixing trend, but the minimum signature is lower than that of Traverse 3.

## 5.5 Traverse 5

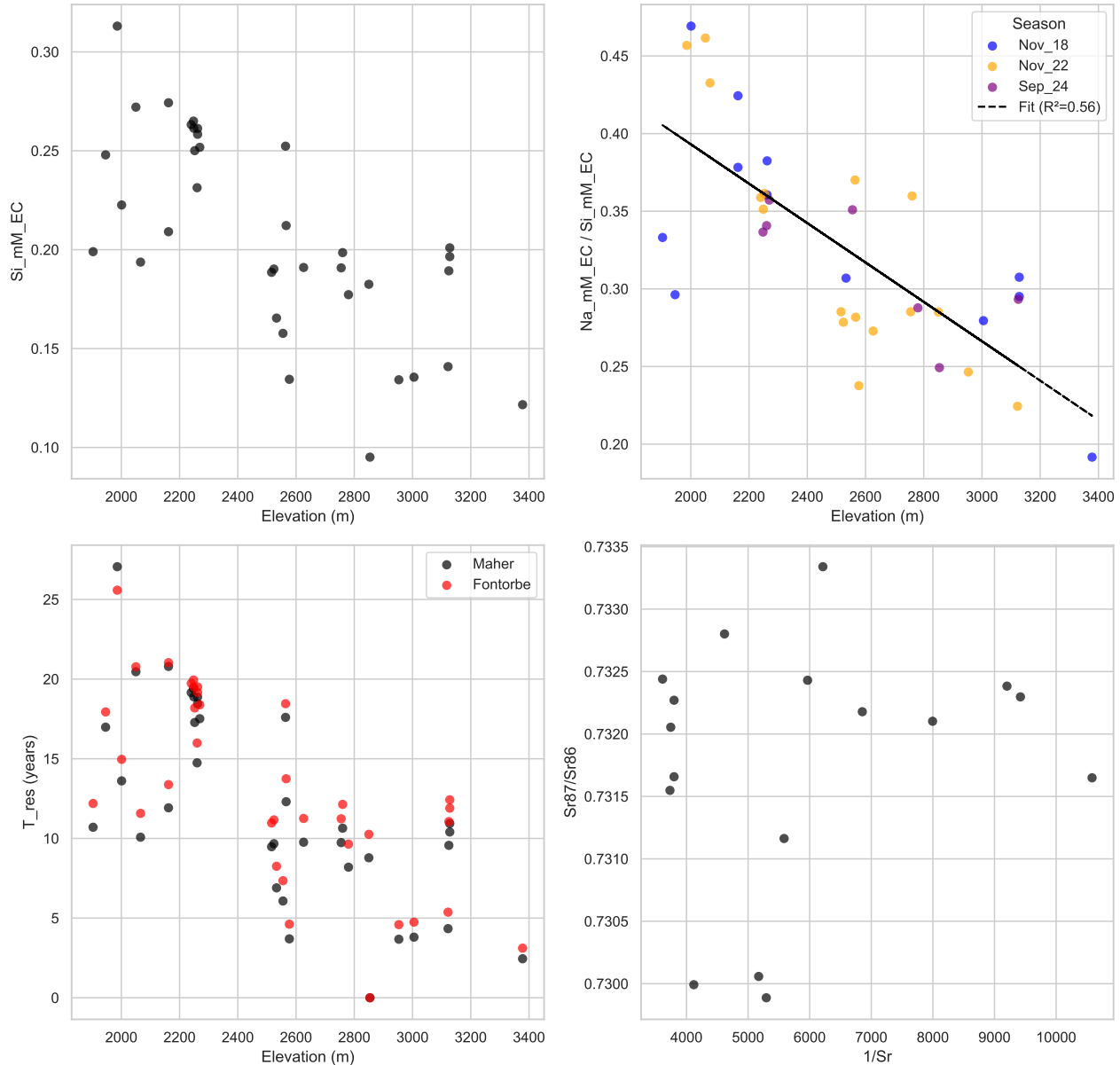


Figure 7: Traverse 5 - Variations in Spatial Chemistry

Traverse 5 is highly sampled and sits at the highest elevation of the whole catchment. DSi concentration increases with decreasing elevation but there is noticeable scatter in the data. Na/Si similarly shows a trend of increasing ratio with decreasing elevation, and it is replicated between different seasons, with considerable scatter. Residence times are the lowest predicted in the catchments, and so are the strontium isotope values.

## 5.6 Time Series Trends

Concentrations of dissolved silicon in several springs in the catchment show a consistent decrease in concentration with the onset of the monsoon. Concentrations are high in April, decrease to a minimum in September, then slowly increase back to April levels through October and November. Decrease in concentration is likely a sign of dilution from increased precipitation during the monsoon. Such a trend is also present in a time series of a spring in Traverse 3. The average April-September decrease is small compared to the average dissolved silicon concentration of the rain.

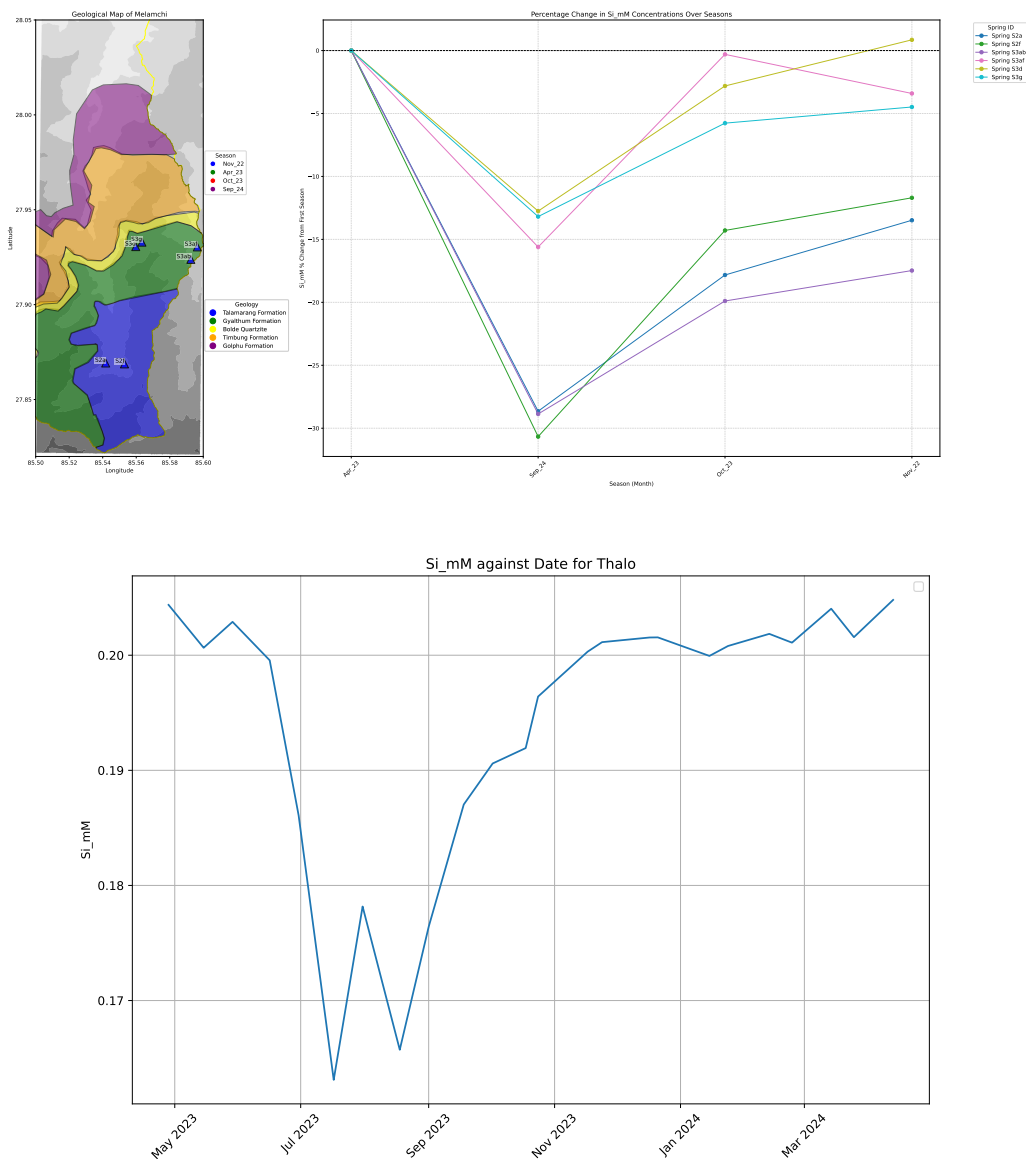


Figure 8: Seasonal changes in spring concentration indicating monsoonal precipitation influence.; Time series of spring concentration changes over time.

## 6 Discussion

### 6.1 Explaining Traversal Variations in Chemistry

Increasing DSi concentration with decreasing elevation suggests the springs are sampling increasingly longer flow paths. This is because longer flow paths allow for more water-rock interaction, which scavenges more Si from the silicate rocks. While most traverses show such a trend, this does not happen in Traverse 1. There are several possible reasons for this. For one, the lowermost springs are likely to be close to the Melamchi river which is more dilute than the most concentrated springs in the traverse. It is unlikely that the decrease is caused by a dilution effect at the start of the monsoon such as that shown in Figure (ref). This is because these DSi trends are consistent across multiple seasons within error. Clearly, however, samples collected in September will be relatively more dilute than those collected in April.

A decrease in Si at lower elevations here could also suggest precipitation of secondary minerals. Linear trends in plot (b?) for Traverses 1, 3, and 5 show an increase in Na/Si as elevation decreases. Si is involved in the backward secondary mineral precipitation weathering reaction, and Na is not, as evidenced in equation (?). In other words, elevated Na/Si is interpreted as a sign of a closer approach to equilibrium, as more Si is scavenged from the water to form secondary precipitates, while the Na is only involved in dissolution. This is consistent with the Traverse 1 springs having the highest concentrations of Si in the catchment as chemical equilibrium is approached.

Plots of Na/Si against elevation coloured by season can also be used to infer how consistently a given flow path is sampled. Because Na/Si is primarily controlled by the balance of dissolution and reprecipitation, and therefore the average age of water in the flow path, consistency of this value over time points to the same flow path length being sampled for a given rate of reaction. Under the steady state assumption assumption  $\partial C / \partial t = 0$  used in the residence time models, the Na/Si ratio should be constant over time at a given ele-

vation if the same flow path is sampled. For both Traverse 3 and 5, the Na/Si ratio against elevation does not change between different seasons. However, there is a better correlation in Traverse 3 which suggests the flow paths here are more consistently sampled.

The consistency with which flow paths are sampled in Traverse 3 is more apparent when plotting Na/Si in one season against the rest (note that Figure 9 the Na/Si values are uncorrected to showcase results collected in more than two seasons).

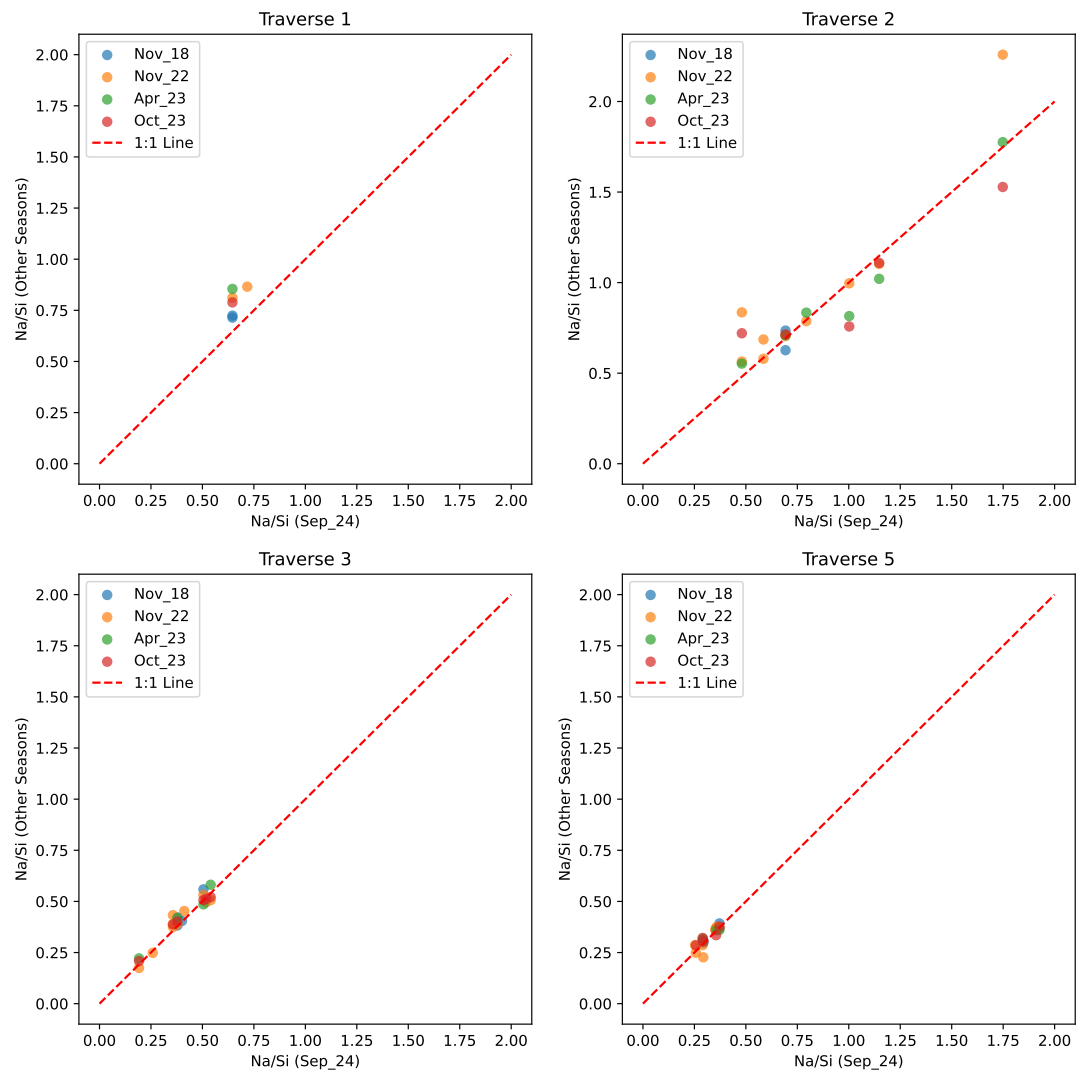


**Figure 9: How Na/Si varies for different traverses. Traverse 4 is not plotted due to the lack of samples.**

The scatter in these plots reflect temporal variability in the spring chemistry. Traverses 1 and 5 both display tight scatter, consistent with the notion that the flow paths here are consistently sampled. More notable here are the differences in Na/Si values between traverses. These show the spatial variability between traverses is more significant than the temporal variability. It is possible, and quite likely that all traverses flow paths are connected one to the other. When investigating model differences, however, a knowledge of which traverse accounts for what discrepancy allows for the contribution of spatial variation toward the overall interpretation to be taken into account.

## 6.2 Strontium Isotopes suggest Little Rainwater Influence

Radiogenic strontium isotope analyses of springs show a wide variation between different traverses. Due to the unique source-tracking nature of strontium isotopes, this is potentially explained with varying lithology (see Appendix / ref). In other words, different traverses sample lithologies that have different strontium isotopic composition, and the water chemistry reflects this. These variations are within the range of Higher Himalayan Crystalline Series (HHCS) rocks found in the region (Tipper et al., 2006). It is unlikely that the source of the Sr isotopes is from the Lesser Himalayan Series (LHS) rocks. Indeed the Main Central Thrust (MCT) is several km south of Melamchi.

Sr isotopes were also measured for the collected rain samples, and these range from 0.70904 to 0.73906. Aside from the rain sample collected in the southern Melamchi valley, the Sr isotope values are consistent with the expected values for rainwater (Galy, France-Lenord, Derry, 1999). Furthermore, the lowest Sr isotope value for rain is very close to the reported value for seawater, which is 0.70917. The lowest rain values therefore likely reflect seawater strontium isotope values, indicating little contamination from dust or particles. The uncontaminated samples are indeed found at the higher elevations, and they show low chloride concentrations consistent with rain.

Strontium isotope ratios used alongside strontium concentrations can be used to de-

<b>Sample ID</b>	<b>Elevation (m)</b>	<b>pH</b>	<b><math>^{87}\text{Sr}/^{86}\text{Sr}</math> (2SD·10<sup>6</sup>)</b>	<b>Sr (<math>\mu\text{M}</math>)</b>	<b>Cl (<math>\mu\text{M}</math>)</b>	<b><math>\delta^{18}\text{O}</math> (%)</b>
NEP24-039	840	6.79	0.73906	(24)	0.13	28.09
NEP24-043	1351	5.82	0.71442	(46)	0.01	3.55
NEP24-044	1952	6.05	0.71352	(127)	0.01	1.89
NEP24-045	2644	5.00	0.71292	(73)	0.01	3.21
NEP24-046	2110	6.02	0.70904	(100)	0.02	2.86
NEP24-047	2644	5.74	0.71194	(237)	0.01	0.55
NEP24-048	2644	5.61	0.71182	(189)	0.01	3.65

**Table 5:** Strontium isotope ratios, chloride and strontium concentrations (in micromolar, M), elevation, pH, and  $\delta^{18}\text{O}$  values (‰ VSMOW). Error (2SD) values are multiplied by 10<sup>6</sup>.

termine mixing between different endmembers (Faure, 1986; See Appendix). Plots of  $\frac{^{87}\text{Sr}}{^{86}\text{Sr}}$  against  $\frac{1}{\text{Sr}}$  that yield straight lines are indicative of mixing trends.

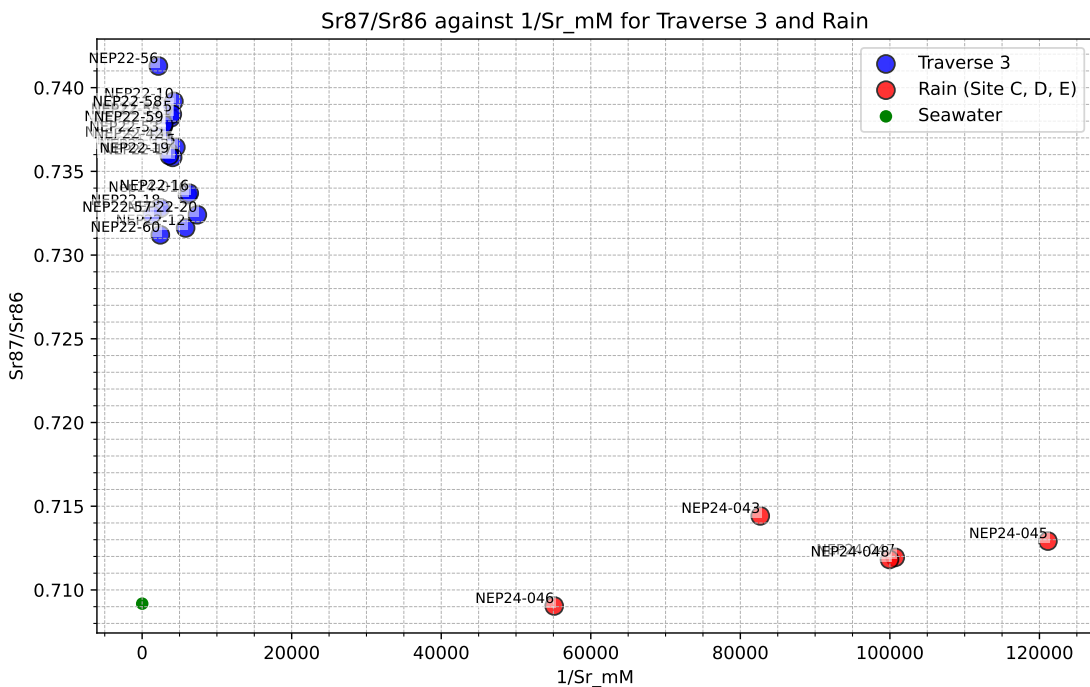
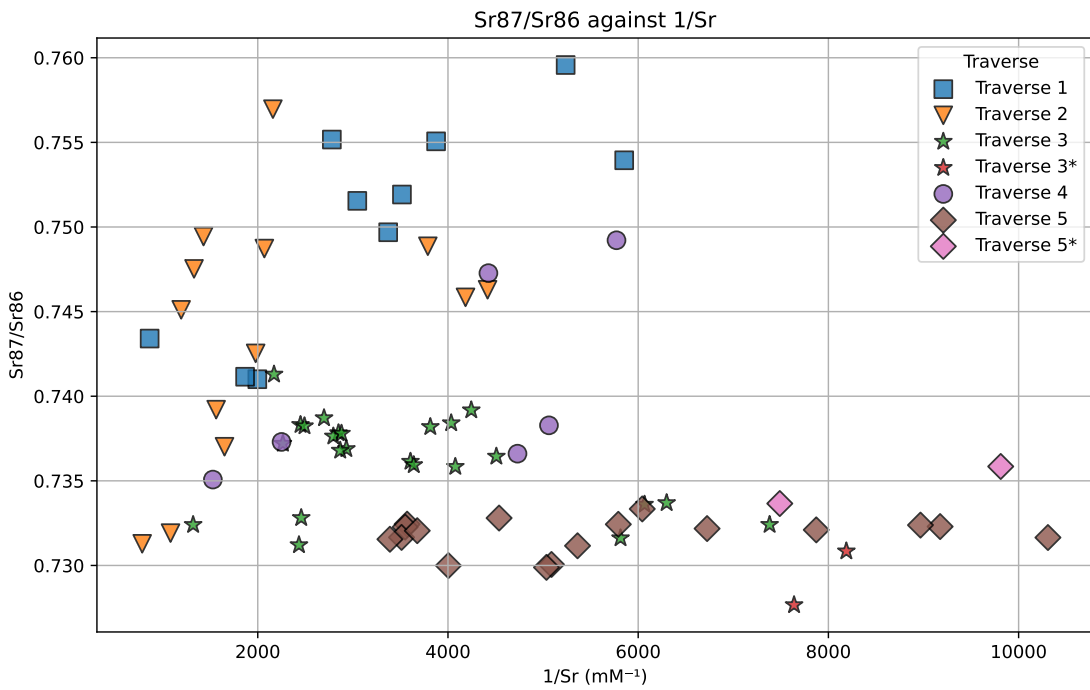


Figure 10: Strontium isotope differences display difference in lithology tapped in. Cite Quade and Tipper papers; Rain analysed for Sr isotopes and Cl. Something about contamination lower down; How samples of Traverse 3 compare to the rain samples

Figure 10a shows  $\frac{^{87}Sr}{^{86}Sr}$  against  $\frac{1}{Sr}$  for springs in the catchment. The plot shows two distinct mixing lines between Traverses 1-3, and Traverses 3-5 [need to draw them on]. This supports that found in figure 4, which suggests the water chemistry in Traverses 1 and 2 is quite different to the trend set by Traverses 3-5. Comparing spring samples to the rain [Change graph], it is clear that the latter does not exert a significant control on the spring chemistry, not even for the presumably shortest flow paths at the top of the ridge. In other words, chemical weathering reactions are likely to be the main control on the spring chemistry.

### 6.3 Model Constraints on Residence Time

Residence times in Traverse 1 are explainably the longest in the catchment. The springs here are at the lowest elevation, so the flow paths are presumably the longest. This is consistent with the highest DSi concentration of the catchment, and evidence for secondary precipitation of kaolinite at the lowest elevations (See Figure ?b). In Traverse 1, the Fontorbe model predicts a peak of  $\approx 100$  years, while the Maher model has a much higher residence time of  $\approx 600$  years. The discrepancy is likely due to how the models are formulated.

Fontorbe	Maher
$T_f = \frac{(C_h - C_o) \cdot \phi}{(1 - f) \cdot R_n}$	$T_f = \frac{C_{eq} \cdot (C - C_0)}{e^2 R_n (C_{eq} - C)}$
$R_n = \frac{(C_h - C_o) \cdot \phi}{(1 - f) \cdot T_f}$	$R_n = \frac{C_{eq} \cdot (C - C_0)}{e^2 T_f (C_{eq} - C)}$

Table 6: Comparison of equations from Fontorbe and Maher

The difference in the models comes from the equilibrium concentration in the Maher formula. Indeed, for this study's formulation, the equilibrium concentration is taken to be the highest in the catchment,  $869 \mu\text{M}$  DSi. This concentration corresponds to a spring in

Traverse 1. Note that in the Maher and Chamberlain (2013) model setup, an equilibrium concentration of  $375\mu\text{M}$  DSi is chosen from the global river data of Gaillardet et al. (1999). This makes sense for a theoretical model but is clearly not appropriate for this catchment. The Fontorbe model, on the other hand, does not depend on the equilibrium concentration. The  $\frac{C_{eq}}{(C_{eq}-C)}$  term in the Maher model gets larger as the concentration approaches equilibrium. As a result of this, the Maher model consistently predicts longer residence times than the Fontorbe Model at higher DSi concentrations, while the opposite is true at lower DSi concentrations. It also follows that for Traverse 1 the  $\frac{C_{eq}}{(C_{eq}-C)}$  term grows arbitrarily large, hence the strong discrepancy found in Figure (?c).

The formulation is different because of how the two models approach rate of reaction. This is constant in the Fontorbe model, and depends on the equilibrium concentration for the Maher model (see Eqn ?). Indeed, as equilibrium concentration is reached in the Maher model, the reaction rate will decrease, and the residence time will increase. It is unrealistic that reaction rate continue to be constant as the reaction progresses, and so the Maher model more accurately reflects water that is close to equilibrium.

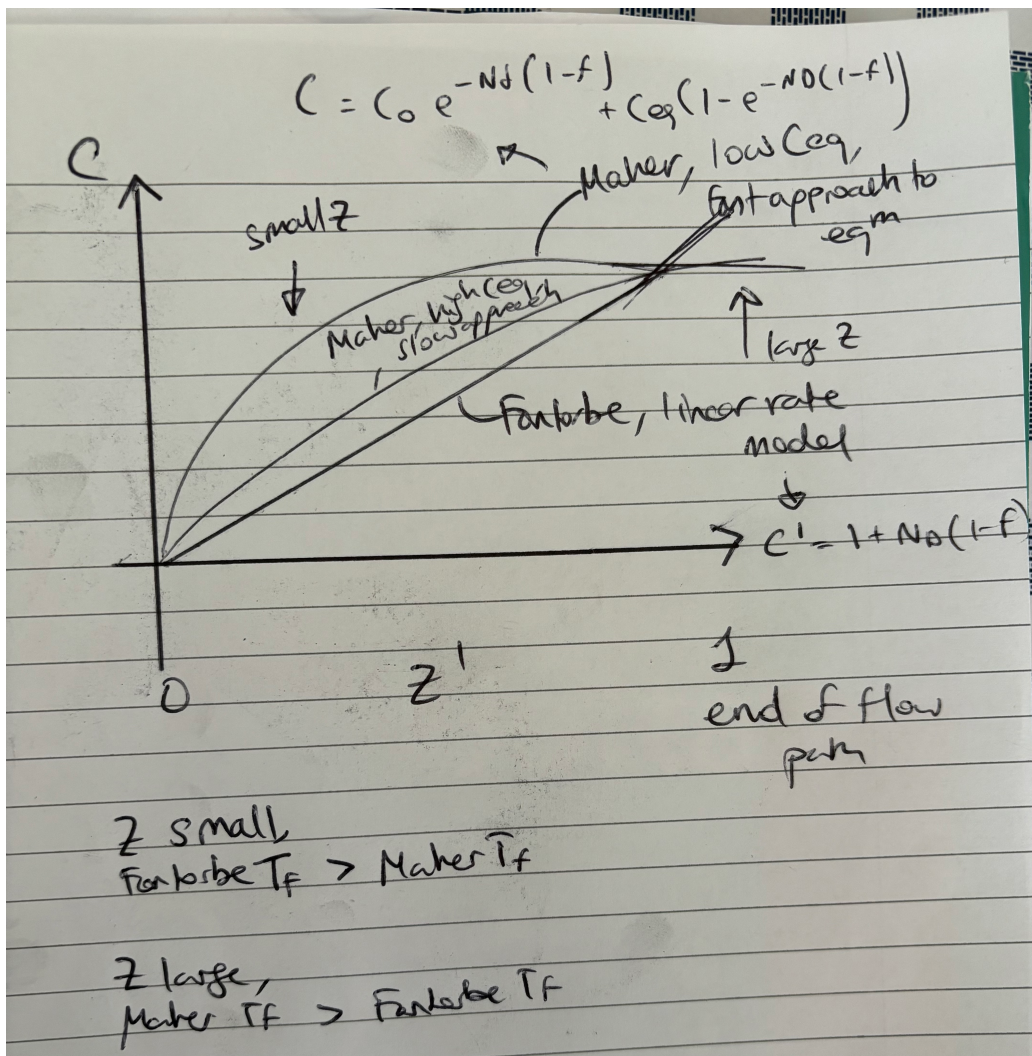


Figure 11: Comparison of how concentration changes with flow path length for the two models, and different equilibrium concentration

There is an argument to be made as to whether it is appropriate to choose the highest DSi concentration in the catchment as the equilibrium concentration. Maher (2011) details several ways in which the Maher model concentrations could change depending on the conditions. For example, increasing PCO<sub>2</sub> would increase the concentration of DSi at equilibrium. This aspect of the testing undergone in this study is therefore not well constrained. A more pressing concern, however, is whether the springwaters sampled are actually close to equilibrium. The free energy of reaction can be used to determine this.

## 6.4 Free Energy Calculations

A further constraint on the approach to equilibrium of a water packet is the free energy of reaction, which can be calculated using the activity of the ions in solution. Free energy is defined as:[cite](#)

$$\Delta G = \Delta G^0 + RT \ln Q \quad (13)$$

The plagioclase to kaolinite reaction is given by equation 4. The parameters for the standard free energy of reaction are calculated using the pygcc python package ([cite](#)). The package gives the standard properties of solid-solution species and reactions, such that  $\Delta G^0$  can be calculated:

$$\Delta G^0 = \Delta G_{products}^0 - \Delta G_{reactants}^0 = -RT \ln K \quad (14)$$

K is calculated using the database obtained from pygcc using The Geochemist's Workbench® Rxn program([ref](#)). Q is calculated as the ion activity product of the reaction, assuming an ideal system whereby the activity is equal to the concentration of the ion in the water **Assuming the activities of the solid phases plagioclase and kaolinite are 1, the activity of water is 1, and the activity of the ions in solution are equal to their concentration, the free energy of reaction can be calculated.**

$$Q = \frac{a_{\text{Kaol}}^{0.6} a_{\text{Na}^+}^{0.8} a_{\text{Ca}^{2+}}^{0.2} a_{\text{SiO}_2(\text{aq})}^{1.6}}{a_{\text{An}_{20}} a_{\text{H}^+}^{1.2}} \quad (15)$$

It is important to note that the composition of the plagioclase is important. The free energy of reaction is lowered by the presence of a solid solution between albite and anorthite (Dubacq, 2022). **In our case...**

## Need to write

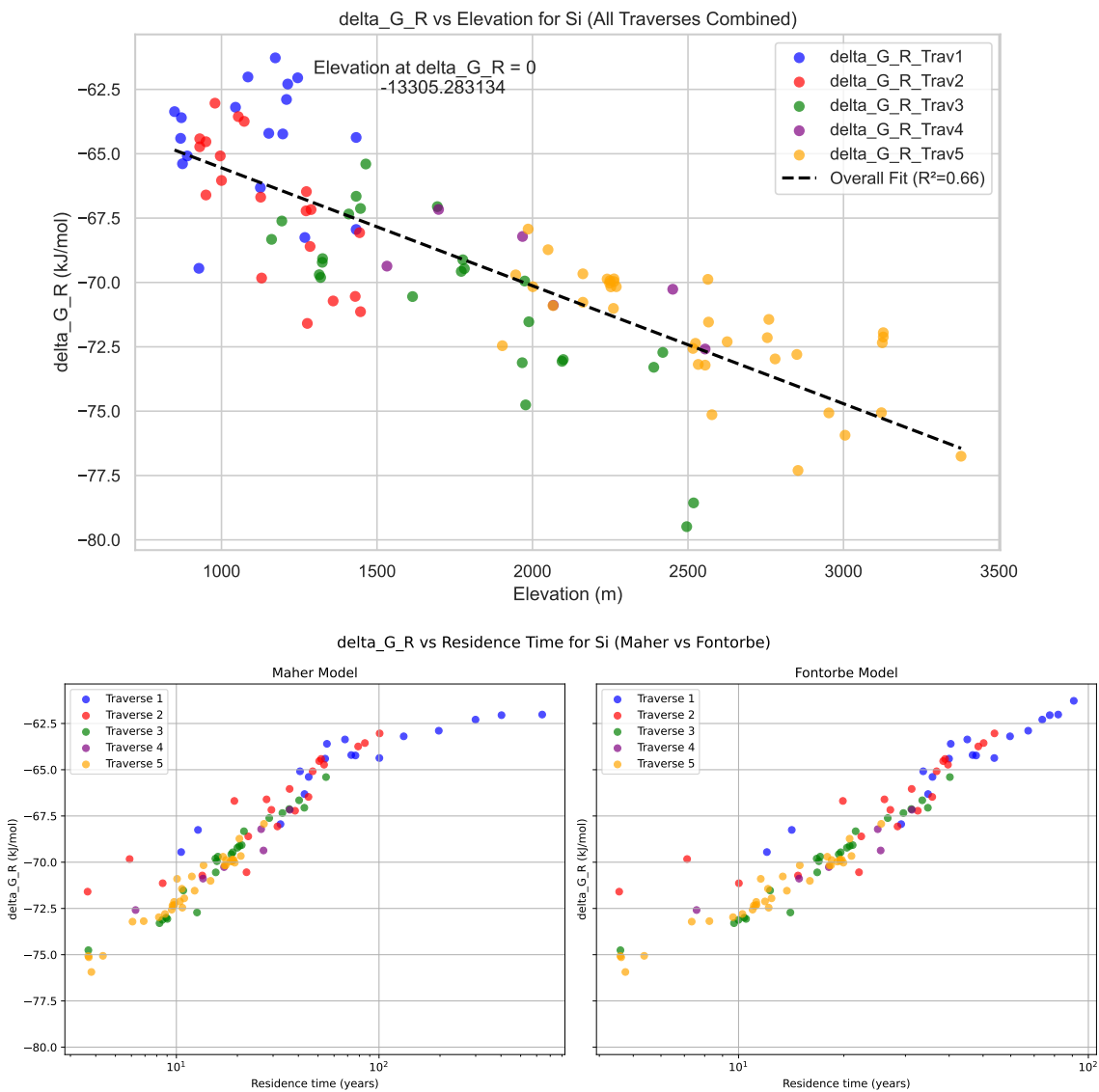


Figure 12: Comparison of the delta G obtained against elevation. Comparison of delta G with residence time for both models

## Constraints on Reaction Rate

Figure 12 shows a decrease in  $\Delta G$  as elevation decreases for all traverses, consistent with water getting closer to equilibrium as the flow path length increases. However, the free energy is only on the order of -60 kJ/mol at the longest flow path. This is not close to the -10kJ/mol that Kampman et al. (2014) suggest is the "near equilibrium plateau". Especially for Traverse 1, this suggests that the  $C_{eq}$  chosen for the Maher model is not appropriate. In order for the Maher model to be accurate in its estimation of residence time and rate of reaction as equilibrium is approached, given the trend in  $\Delta G$ , the equilibrium concentration should be much higher than 869  $\mu\text{M}$  DSi, on the order of five times as much.

There might be an argument, also, to suggest that the reaction rate is not as high as the models suggest. Indeed, at those values, laboratory rates might be more appropriate  
**Have the Kampman table? Lab rates of reaction are much faster for this**. One sure test is to compare the free energy obtained for the samples in Traverse 3 to those in Traverse 1. Given that the equilibrium concentration for the residence time is taken from this latter traverse (see Figure in results, ref), according to the formulation of the Maher model this should be closest to equilibrium.

Hence, it is likely that a larger reaction rate is needed to characterise these groundwaters. This has implications for the residence times calculated using these models, as the former and latter are inversely proportional.

**Bit about Maher assuming equilibrium reached -> Maher not correct to implement here.  
Also mike permeability sketch???**

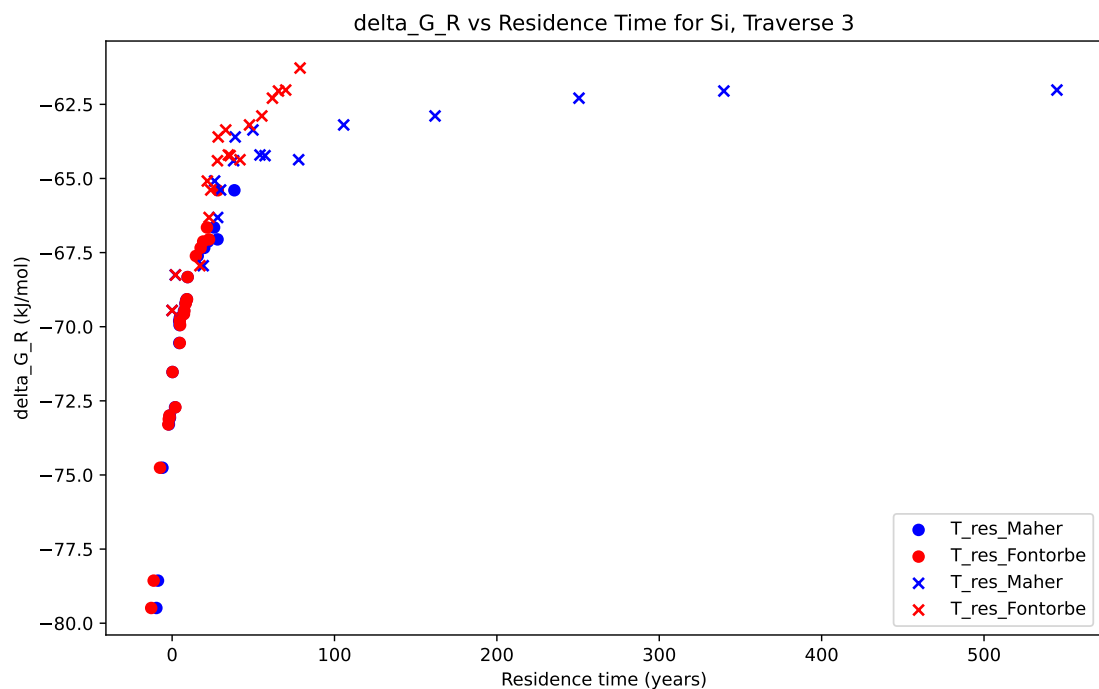
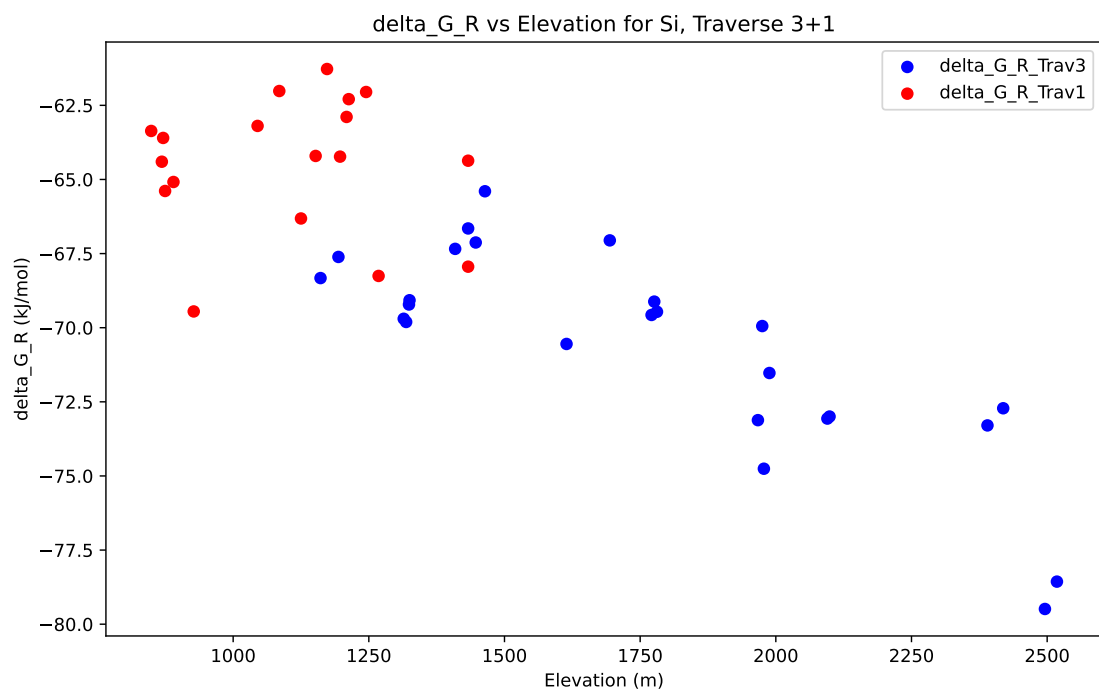


Figure 13: Comparison of the delta G obtained against elevation for Traverse 1 and Traverse 3. And residence time comparison, Note how Maher predicts really high residence times when Ceq is approached

## References

- [1] Open-file report. Series: Open-File Report.
- [2] Sunil Acharya, Xiaoxin Yang, Tandong Yao, and Dibas Shrestha. Stable isotopes of precipitation in nepal himalaya highlight the topographic influence on moisture transport. 565:22–30.
- [3] Tirtha Raj Adhikari, Binod Baniya, QiuHong Tang, Rocky Talchabhadel, Manish Raj Gouli, Bhumi Raj Budhathoki, and Ram Prasad Awasthi. Evaluation of post extreme floods in high mountain region: A case study of the melamchi flood 2021 at the koshi river basin in nepal. 3(3):437–446.
- [4] Christoff Andermann, Laurent Longuevergne, Stéphane Bonnet, Alain Crave, Philippe Davy, and Richard Gloaguen. Impact of transient groundwater storage on the discharge of himalayan rivers. 5(2):127–132.
- [5] C. A. J. Appelo and Dieke Postma. Geochemistry, groundwater and pollution. CRC Press, 2nd ed., 5th corr. repr edition.
- [6] Abra Catherine Atwood. Critical zone response to perturbation: from mountain building to wildfire.
- [7] Binod Baniya, QiuHong Tang, Tirtha Raj Adhikari, Gang Zhao, Gebremedhin Gebremeskel Haile, Madan Sigdel, and Li He. Climate change induced melamchi extreme flood and environment implication in central himalaya of nepal. 120(12):11009–11029.
- [8] Paolo Benettin, Scott W. Bailey, John L. Campbell, Mark B. Green, Andrea Rinaldo, Gene E. Likens, Kevin J. McGuire, and Gianluca Botter. Linking water age and solute dynamics in streamflow at the hubbard brook experimental forest, NH, USA. 51(11):9256–9272.

- [9] Craig M Bethke. GEOCHEMICAL AND BIOGEOCHEMICAL REACTION MODELING, second edition.
- [10] M.J. Bickle, E. Tipper, A. Galy, H. Chapman, and N. Harris. On discrimination between carbonate and silicate inputs to himalayan rivers. 315(2):120–166.
- [11] Bodo Bookhagen and Douglas W. Burbank. Toward a complete himalayan hydrological budget: Spatiotemporal distribution of snowmelt and rainfall and their impact on river discharge. 115:2009JF001426.
- [12] Jesús Carrera, Maarten W. Saaltink, Joaquim Soler-Sagarra, Jingjing Wang, and Cristina Valhondo. Reactive transport: A review of basic concepts with emphasis on biochemical processes. 15(3):925.
- [13] Mingkun Chen, Lei Gong, Jacques Schott, Peng Lu, Kaiyun Chen, Honglin Yuan, Jian Sun, Si Athena Chen, John Apps, and Chen Zhu. Coupled feldspar dissolution and secondary mineral precipitation in batch systems: 6. labradorite dissolution, calcite growth, and clay precipitation at 60 °c and pH 8.2–8.4. 390:181–198.
- [14] Christian David, Teng-Fong Wong, Wenlu Zhu, and Jiaxiang Zhang. Laboratory measurement of compaction-induced permeability change in porous rocks: Implications for the generation and maintenance of pore pressure excess in the crust. 143(1):425–456.
- [15] Megh Raj Dhital. Geology of the Nepal Himalaya. Regional Geology Reviews. Springer International Publishing.
- [16] Jennifer L. Druhan and Kate Maher. The influence of mixing on stable isotope ratios in porous media: A revised rayleigh model. 53(2):1101–1124.
- [17] Benoît Dubacq. Thermodynamics of ordering and mixing in plagioclase feldspars: atomistic modelling in favour of landau theory. 177(10):102.
- [18] Guillaume Fontorbe, Christina L. De La Rocha, Hazel J. Chapman, and Michael J. Bickle. The silicon isotopic composition of the ganges and its tributaries. 381:21–30.

- [19] J. Gaillardet, B. Dupré, P. Louvat, and C.J. Allègre. Global silicate weathering and CO<sub>2</sub> consumption rates deduced from the chemistry of large rivers. 159(1):3–30.
- [20] Albert Galy, Christian France-Lanord, and Louis A Derry. The strontium isotopic budget of himalayan rivers in nepal and bangladesh. 63(13):1905–1925.
- [21] R.B. Georg, B.C. Reynolds, A.J. West, K.W. Burton, and A.N. Halliday. Silicon isotope variations accompanying basalt weathering in iceland. 261(3):476–490.
- [22] R.B. Georg, B.C. Reynolds, A.J. West, K.W. Burton, and A.N. Halliday. Silicon isotope variations accompanying basalt weathering in iceland. 261(3):476–490.
- [23] Jon K. Golla, Marie L. Kuessner, Michael J. Henehan, Julien Bouchez, Daniella M. Rempe, and Jennifer L. Druhan. The evolution of lithium isotope signatures in fluids draining actively weathering hillslopes. 567:116988.
- [24] Bradley W. Goodfellow, George E. Hilley, Samuel M. Webb, Leonard S. Sklar, Seulgi Moon, and Christopher A. Olson. The chemical, mechanical, and hydrological evolution of weathering granitoid. 121(8):1410–1435.
- [25] Emma L. S. Graf, Hugh D. Sinclair, Mikael Attal, Boris Gailleton, Basanta Raj Adhikari, and Bishnu Raj Baral. Geomorphological and hydrological controls on sediment export in earthquake-affected catchments in the nepal himalaya.
- [26] Danielle K. Hare, Ashley M. Helton, Zachary C. Johnson, John W. Lane, and Martin A. Briggs. Continental-scale analysis of shallow and deep groundwater contributions to streams. 12(1):1450.
- [27] Madeline M Hille. The orographic influence on storm variability, extreme rainfall characteristics and rainfall-triggered landsliding in the central nepalese himalaya.
- [28] T.J. B. Holland and R. Powell. An improved and extended internally consistent thermodynamic dataset for phases of petrological interest, involving a new equation of state for solids: THERMODYNAMIC DATASET FOR PHASES OF PETROLOGICAL INTEREST. 29(3):333–383.

- [29] L. Illien, C. Andermann, C. Sens Schönfelder, K. L. Cook, K. P. Baidya, L. B. Adhikari, and N. Hovius. Subsurface moisture regulates himalayan groundwater storage and discharge. 2(2):e2021AV000398.
- [30] Scott Jasechko. Global isotope hydrogeology review. 57(3):835–965.
- [31] Scott Jasechko. Partitioning young and old groundwater with geochemical tracers. 427:35–42.
- [32] A. Joshua West, Mike J. Bickle, Rob Collins, and James Brasington. Small-catchment perspective on himalayan weathering fluxes. 30(4):355.
- [33] Pratik Kad and Kyung Ja Ha. Recent tangible natural variability of monsoonal orographic rainfall in the eastern himalayas. 128(22):e2023JD038759.
- [34] Niko Kampman, Mike Bickle, John Becker, Nelly Assayag, and Hazel Chapman. Feldspar dissolution kinetics and gibbs free energy dependence in a CO<sub>2</sub>-enriched groundwater system, green river, utah. 284(3):473–488.
- [35] D. B. Kattel, T. Yao, K. Yang, L. Tian, G. Yang, and D. Joswiak. Temperature lapse rate in complex mountain terrain on the southern slope of the central himalayas. 113(3):671–682.
- [36] Julia L. A. Knapp, Colin Neal, Alessandro Schlumpf, Margaret Neal, and James W. Kirchner. New water fractions and transit time distributions at plynlimon, wales, estimated from stable water isotopes in precipitation and streamflow. 23(10):4367–4388.
- [37] Alasdair C.G. Knight, Emily I. Stevenson, Luke Bridgestock, J. Jotautas Baronas, William J. Knapp, Basanta Raj Adhikari, Christoff Andermann, and Edward T. Tipper. The impact of adsorption–desorption reactions on the chemistry of himalayan rivers and the quantification of silicate weathering rates. 641:118814.
- [38] Lee R. Kump, Susan L. Brantley, and Michael A. Arthur. Chemical weathering, atmospheric CO<sub>2</sub>, and climate. 28(1):611–667.

- [39] Başak Kısakürek, Rachael H. James, and Nigel B.W. Harris. Li and  $\delta^{7Li}$  in himalayan rivers: Proxies for silicate weathering? 237(3):387–401.
- [40] K. Maher. The dependence of chemical weathering rates on fluid residence time. 294(1):101–110.
- [41] K. Maher. The role of fluid residence time and topographic scales in determining chemical fluxes from landscapes. 312(1):48–58.
- [42] K. Maher and C. P. Chamberlain. Hydrologic regulation of chemical weathering and the geologic carbon cycle. 343(6178):1502–1504.
- [43] K. Maher and C. P. Chamberlain. Hydrologic regulation of chemical weathering and the geologic carbon cycle. 343(6178):1502–1504.
- [44] Kate Maher, Carl I. Steefel, Art F. White, and Dave A. Stonestrom. The role of reaction affinity and secondary minerals in regulating chemical weathering rates at the santa cruz soil chronosequence, california. 73(10):2804–2831.
- [45] Katharine Maher, Donald J. DePaolo, and Jo Chiu-Fang Lin. Rates of silicate dissolution in deep-sea sediment: In situ measurement using  $^{234}U/^{238}U$  of pore fluids. 68(22):4629–4648.
- [46] Odin Marc, Robert Behling, Christoff Andermann, Jens M. Turowski, Luc Illien, Sigrid Roessner, and Niels Hovius. Long-term erosion of the nepal himalayas by bedrock landsliding: the role of monsoons, earthquakes and giant landslides. 7(1):107–128.
- [47] James L. McCallum, Peter G. Cook, and Craig T. Simmons. Limitations of the use of environmental tracers to infer groundwater age. 53:56–70.
- [48] K. J. McGuire, J. J. McDonnell, M. Weiler, C. Kendall, B. L. McGlynn, J. M. Welker, and J. Seibert. The role of topography on catchment scale water residence time. 41(5):2004WR003657.
- [49] William G. Medwedeff, Marin K. Clark, Dimitrios Zekkos, A. Joshua West, and Deepak Chamlagain. Near surface geomechanical properties and weathering char-

acteristics across a tectonic and climatic gradient in the central nepal himalaya. 127(2):e2021JF006240.

- [50] Jeeban Panthi, Piyush Dahal, Madan Shrestha, Suman Aryal, Nir Krakauer, Soni Pradhanang, Tarendra Lakhankar, Ajay Jha, Mohan Sharma, and Ramchandra Karki. Spatial and temporal variability of rainfall in the gandaki river basin of nepal himalaya. 3(1):210–226.
- [51] Michelle A. Pedrazas, W. Jesse Hahm, Mong Han Huang, David Dralle, Mariel D. Nelson, Rachel E. Breunig, Kristen E. Fauria, Alexander B. Bryk, William E. Dietrich, and Daniella M. Rempe. The relationship between topography, bedrock weathering, and water storage across a sequence of ridges and valleys. 126(4):e2020JF005848.
- [52] Jay Quade, Nathan English, and Peter G DeCelles. Silicate versus carbonate weathering in the himalaya: a comparison of the arun and seti river watersheds. 202(3):275–296.
- [53] Kevin Roback, Marin K. Clark, A.Joshua West, Dimitrios Zekkos, Gen Li, Sean F. Gallen, Deepak Chamlagain, and Jonathan W. Godt. The size, distribution, and mobility of landslides caused by the 2015 mw7.8 gorkha earthquake, nepal. 301:121–138.
- [54] Joaquim Soler-Sagarra, Maarten W. Saaltink, Francesca De Gaspari, Albert Nardi, and Jesús Carrera. Water mixing approach (WMA) for reactive transport modeling.
- [55] Matthias Sprenger, Christine Stumpp, Markus Weiler, Werner Aeschbach, Scott T. Allen, Paolo Benettin, Maren Dubbert, Andreas Hartmann, Markus Hrachowitz, James W. Kirchner, Jeffrey J. McDonnell, Natalie Orlowski, Daniele Penna, Stephan Pfahl, Michael Rinderer, Nicolas Rodriguez, Maximilian Schmidt, and Christiane Werner. The demographics of water: A review of water ages in the critical zone. 57(3):800–834.
- [56] R. F. Stallard and J. M. Edmond. Geochemistry of the amazon: 2. the influence of geology and weathering environment on the dissolved load. 88:9671–9688.

- [57] Philip A. E. Pogge Von Strandmann, Mathieu Dellinger, and A. Joshua West. Lithium Isotopes: A Tracer of Past and Present Silicate Weathering. Cambridge University Press, 1 edition.
- [58] Nicholas E. Thiros, Erica R. Siirila Woodburn, P. James Dennedy Frank, Kenneth H. Williams, and W. Payton Gardner. Constraining bedrock groundwater residence times in a mountain system with environmental tracer observations and bayesian uncertainty quantification. 59(2):e2022WR033282.
- [59] Edward T Tipper. The isotopic fingerprint of calcium and magnesium: from the alteration of the continental crust to global budgets.
- [60] Edward T. Tipper, Mike J. Bickle, Albert Galy, A. Joshua West, Catherine Pomiès, and Hazel J. Chapman. The short term climatic sensitivity of carbonate and silicate weathering fluxes: Insight from seasonal variations in river chemistry. 70(11):2737–2754.
- [61] Rong Wen, LiDe Tian, YongBiao Weng, ZhongFang Liu, and ZhongPing Zhao. The altitude effect of  $\delta$  18O in precipitation and river water in the southern himalayas. 57(14):1693–1698.
- [62] A West, A Galy, and M Bickle. Tectonic and climatic controls on silicate weathering. 235(1):211–228.
- [63] A. J. West, M. Arnold, G. Aumaître, D. L. Bourlès, K. Keddadouche, M. Bickle, and T. Ojha. High natural erosion rates are the backdrop for present-day soil erosion in the agricultural middle hills of nepal. 3(3):363–387.
- [64] Art F. White, Alex E. Blum, Marjorie S. Schulz, Tom D. Bullen, Jennifer W. Harden, and Maria L. Peterson. Chemical weathering rates of a soil chronosequence on granitic alluvium: I. quantification of mineralogical and surface area changes and calculation of primary silicate reaction rates. 60(14):2533–2550.
- [65] Art F White and Susan L Brantley. The effect of time on the weathering of silicate minerals: why do weathering rates differ in the laboratory and field? 202(3):479–506.

- [66] John A Wojtowicz. The thermodynamic basis of the saturation index.
- [67] Bing Xu, Aihong Xie, and Jiangping Zhu. Can water vapor transport over the himalayas above 8000 m asl?—a case study on mt. everest. 14(11):1671.

## Appendix 1: Strontium Isotopes Mass Balance Mixing Model

Following Faure (2001 - Origin of Igneous Rocks), the Sr concentrations of a two-component mixture can be expressed as:

$$[Sr]_M = [Sr]_A f_A + [Sr]_B (1 - f_A) \quad (16)$$

These are related to the isotopic composition with:

$$\left( \frac{^{87}Sr}{^{86}Sr} \right)_M = \left( \frac{^{87}Sr}{^{86}Sr} \right)_A f_A \frac{[Sr]_A}{[Sr]_M} + \left( \frac{^{87}Sr}{^{86}Sr} \right)_B (1 - f_A) \frac{[Sr]_B}{[Sr]_M} \quad (17)$$

These equations can be combined, yielding:

$$\left( \frac{^{87}Sr}{^{86}Sr} \right)_M = \frac{a}{[Sr]_M} + b; \quad \text{with:} \quad (18)$$

$$a = \frac{[Sr]_A [Sr]_B \left[ \left( \frac{^{87}Sr}{^{86}Sr} \right)_B - \left( \frac{^{87}Sr}{^{86}Sr} \right)_A \right]}{[Sr]_A - [Sr]_B} \quad (19)$$

$$b = \frac{[Sr]_A \left( \frac{^{87}Sr}{^{86}Sr} \right)_A - [Sr]_B \left( \frac{^{87}Sr}{^{86}Sr} \right)_B}{[Sr]_A - [Sr]_B} \quad (20)$$

Plots of  $\frac{^{87}Sr}{^{86}Sr}$  against  $\frac{1}{Sr}$  that yield straight lines are therefore indicative of mixing trends.

## Appendix 2: Rain and Hydrothermal Correction Equations

Spring water is corrected for rain input according to the average concentration for the closest rain sample collected in this field season. To remove the contribution of the rain the following formula is used for any element X:

$$[X]_{rain-corrected} = [X]_{river} - (Cl_{river} - Cl_{river}^*) \frac{[X]_{rain}}{Cl_{rain}} \quad (21)$$

$$Cl_{river}^* = Cl_{river} - Cl_{rain}; \quad \text{if } Cl_{river} > Cl_{rain} \quad (22)$$

Where  $[Cl]_{river}^*$  is calculated by subtracting the concentration of chloride in the rain from that in the river (Tipper et al, 2006).  $Cl^*$  is taken to be zero if the concentration of chloride in the rain is greater than concentration of river. Evapotranspiration is not considered by this model, and studies which show that it plays a minor role, accounting for less than 10% of the hydrological budget in the Himalayas (Andermann et al (2012); Bookhagen and Burbank, 2010). In those cases where  $Cl^*$  is not zero then, a primary rain correction is simply:

$$[X]_{rain-corrected} = [X]_{river} - [X]_{rain} \quad (23)$$

Once the samples have been corrected for rain input, the remaining  $[Cl]^-$  is assumed to be derived from hydrothermal springs encountered in the flow path. This is likely to be the case in one of the southern traverses (Traverse 2) in Melamchi which display high chloride concentrations even after the cyclic correction. Hence, the sample with the highest  $[Cl]^-$  is used to correct:

$$[X]_{hydrothermal-corrected} = [X]_{rain-corrected} - \frac{[X]}{[Cl]_{highest-Cl}} * [Cl]_{rain-corrected} \quad (24)$$

This ensures that all chloride in the corrected sample is removed. The correction uses ionic ratios from the most concentrated water source, which acts as a proxy for the sediment imparting its signature. In this way, the correction does not affect samples which do not have high Cl (and hence do not have a large hydrothermal contribution), but does decrease the concentration of ions for those that do. In the following sections, samples are plotted with the evaporite correction applied where possible. Only in those cases where no chloride was measured is the evaporite correction not applied.

## Appendix 3: Derivation of Reactive Transport Models

### Fontorbe et al. (2013) - Null Hypothesis - Model Derivation

---

This model investigates silicon isotopic composition in the Ganges River, assuming constant reaction rates along flow paths.

The first-order differential equation governing transport and reaction is given as:

To simplify, we introduce non-dimensional variables:

Rewriting Equation (1) using these new variables:

$$\phi \frac{\partial C}{\partial t} = -\omega \phi \frac{\partial C}{\partial z} + R_n(1-f) \quad (25)$$

$$C' = \frac{C}{C_o}, \quad z' = \frac{z}{h}, \quad t' = \frac{t\omega}{h} \quad (26)$$

The Damköhler number ( $N_D$ ) describes the relative importance of kinetic vs transport-controlled settings (Bethke, 2008):

$$N_D = \frac{R_n h}{\phi C_o \omega} \quad (28)$$

Assuming a quasi-stationary state ( $\partial C'/\partial t' = 0$ ), we get:

$$C' = 1 + z' N_D(1-f) \quad (29)$$

At the end of the flow path ( $z = h, z' = 1$ ), this simplifies to:

$$N_D = \frac{C' - 1}{1 - f} \quad (30)$$

The residence time of water along the flow path is:

$$T_f = \frac{h}{\omega} \quad (31)$$

At the end of the flow path:

$$\frac{R_n h}{\phi C_o \omega} = \frac{C' - 1}{1 - f} \quad (32)$$

$$\frac{R_n T_f}{\phi C_o} = \frac{C' - 1}{1 - f} \quad (33)$$

Solving for residence time  $T_f$  and reaction rate  $R_n$ :

$$T_f = \frac{(C - C_o)\phi}{(1 - f)R_n} \quad (34)$$

$C$  is the concentration at the end of the flow path, which is taken to be equal to the concentration of each spring, assuming each spring represents a unique flow path. Note that given these units, the calculation gives time in  $10^{-3}$ s. This is converted to years for practical use.

<b>Fontorbe</b>			
<b>Parameter</b>	<b>Definition</b>	<b>Units</b>	<b>Formula (Value)</b>
$\phi$	Porosity	-	0.1*
$\omega$	Fluid velocity	m/s	Variable
$h$	Length of flow path	m	Variable
$C$	Concentration end of flow path	$\mu\text{mol/L}$	Variable
$C_0$	Initial concentration	$\mu\text{mol/L}$	Rain Input
$f$	Fraction reprecipitated	-	0.5*
$N_D$	Damkohler Number	-	$N_D = \frac{R_n h}{\phi C_0 \omega}$
$T_f$	Residence time	s	$T_f = \frac{h}{\omega \phi}$
$R_n$	Reaction rate	$\text{mol}/\text{m}^3/\text{s}$	$\rho \cdot 10^6 \cdot k \cdot S \cdot X$
$k$	Reaction rate constant	$\text{mol}/\text{m}^2/\text{s}$	$10^{-15*}$
$S$	Specific surface area	$\text{m}^2/\text{g}$	0.1*
$\rho$	Plagioclase density	$\text{g}/\text{cm}^3$	2.7*
$X$	Volume fraction of mineral in rock	$g_{\text{min}}/g_{\text{rock}}$	0.2*

Table 7: Key parameters and definitions for the Fontorbe model. Starred terms are values used for calculation.

## Maher Model Derivation

---

This model describes a reaction-based approach to solute transport, following Maher and Chamberlain (2011, 2014). Maher (2011) suggests a dissolution rate law which decreases linearly to zero at equilibrium. The first-order differential equation governing transport and reaction is:

$$\frac{dC}{dt} = -\frac{q}{\theta} \frac{dC}{dz} + \sum_i \mu_i R_{d,i} \left( 1 - \left( \frac{C}{C_{eq}} \right)^{n_i} \right)^{m_i} - \sum_i \mu_i R_{p,i} \left( 1 - \left( \frac{C}{C_{eq}} \right)^{n_i} \right)^{m_i} \quad (35)$$

Where  $C$  is the concentration,  $q$  is the fluid flux,  $\theta$  is the volumetric water content,  $z$  is the position along the flow path,  $\mu$  is the stoichiometric coefficient,  $R$  is the rate of reaction for dissolution and precipitation respectively,  $C_{eq}$  is the equilibrium concentration, and  $n$  and  $m$  are non-linear parameters (Maher and Chamberlain, 2013). Defining the net reaction rate for a set of packets  $i$ :

$$R_n = \sum_i \mu_i R_{d,i} - \sum_i \mu_i R_{p,i} \quad (36)$$

Maher and Chamberlain describe that the reaction rate decreases linearly with approach to equilibrium.

$$\frac{dc}{dt} = R_n \left( 1 - \frac{C}{C_{eq}} \right) \quad (37)$$

Solving for  $C$ , following Maher and Chamberlain (2013):

$$C = C_0 \exp \left( -\frac{R_n \theta h}{q C_{eq}} \right) + C_{eq} \left( 1 - \exp \left( -\frac{R_n \theta h}{q C_{eq}} \right) \right) \quad (38)$$

The residence time  $T_f$  is defined as:

$$T_f = \frac{h \phi}{q} \quad (39)$$

Thus, at residence time  $T_f$ :

$$c(T_f) = c_0 \exp \left( -\frac{R_n T_f}{c_{eq}} \right) + c_{eq} \left( 1 - \exp \left( -\frac{R_n T_f}{c_{eq}} \right) \right) \quad (40)$$

Following Maher and Chamberlain (2014), this can be rewritten as:

$$C = \frac{C_0}{1 + \tau D_w / q} + C_{eq} \frac{\tau D_w / q}{1 + \tau D_w / q} \quad (41)$$

Where:

$$\tau = e^2; \quad D_w = \frac{h \theta R_n}{C_{eq}} \quad (42)$$

Rewriting the equation:

$$C = \frac{C_0 + C_{\text{eq}} \cdot T_f (e^2 \cdot R_n / C_{\text{eq}})}{1 + T_f (e^2 \cdot R_n / C_{\text{eq}})} \quad (43)$$

Solving for residence time  $T_f$ :

$$T_f = \frac{C_{\text{eq}} \cdot (C - C_0)}{e^2 R_n (C_{\text{eq}} - C)} \quad (44)$$

Note that given these units, the calculation gives time in  $10^{-3}$ s. This is converted to years for practical use. Also note the  $e^2$  term is used because the Maher model considers all paths as if they approach equilibrium.

<b>Maher</b>			
<b>Parameter</b>	<b>Definition</b>	<b>Units</b>	<b>Formula (Value)</b>
$\phi$	Porosity	-	0.1*
$h$	Length of flow path	m	Variable
$q$	Flow rate	m/s	Variable
$C_{\text{eq}}$	Equilibrium concentration	$\mu\text{mol/L}$	Max Catchment
$C_0$	Initial concentration	$\mu\text{mol/L}$	Rain Input
$R_n$	Net reaction rate	$\text{mol/L/s}$	$\rho \cdot 10^6 \cdot k \cdot S \cdot X$
$\rho$	Plagioclase density	$\text{g/cm}^3$	2.7*
$k$	Reaction rate constant	$\text{mol/m}^2/\text{s}$	$10^{-15*}$
$S$	Specific surface area	$\text{m}^2/\text{g}$	0.1*
$X$	Volume fraction of mineral in rock	$g_{\text{min}}/g_{\text{rock}}$	0.2*
$\tau$	Scaling factor	-	$\tau = e^2$
$D_w$	Damkohler Coefficient	$\text{m}^2/\text{s}$	$D_w = \frac{L\phi R_n}{C_{\text{eq}}}$
$T_f$	Residence time	s	$T_f = \frac{h\phi}{q}$

Table 8: Key parameters and definitions for the Maher model. Starred terms are values used for calculation.